ICFO-The Institute of Photonic Sciences

Doctoral Thesis

Optomechanical resonators based on transition metal dichalcogenide monolayers

Author:
Nicolás Morell Bennasser

Supervisor:
Prof. Adrian Bachtold

A thesis submitted in fulfillment of the requirements for the degree of Doctor of Photonics

in the

Quantum Nanomechanics Group

November 12, 2018

Abstract

Suspended monolayer transition metal dichalcogenides (TMD) are membranes that combine ultralow mass and exceptional optical properties, making them intriguing materials for opto-mechanical applications. However, the low measured quality factor of TMD resonators has been a roadblock so far. In this thesis, we first show an ultrasensitive optical readout of monolayer TMD resonators that allows us to reveal their mechanical properties at cryogenic temperatures. We find that the quality factor of monolayer WSe_2 resonators greatly increases below room temperature, reaching values as high as 1.6×10^4 at liquid nitrogen temperature and 4.7×10^4 at liquid helium temperature. This surpasses the quality factor of monolayer graphene resonators with similar surface areas. Upon cooling the resonator, the resonant frequency increases significantly due to the thermal contraction of the WSe_2 lattice. These measurements allow us to experimentally study the thermal expansion coefficient of WSe_2 monolayers for the first time. High Q-factors are also found in resonators based on MoS_2 and $MoSe_2$ monolayers. The high quality-factor found in this work opens new possibilities for coupling mechanical vibrational states to two-dimensional excitons, valley pseudospins, and single quantum emitters and for quantum opto-mechanical experiments based on the Casimir interaction.

The sensing capabilities offered by these high Q-factor nanomechanical oscillators are also of interest for studying thermodynamic properties in condensed matter regimes that are difficult to access. In the second part of the thesis, we use optomechanical systems based on a $MoSe_2$ monolayer to probe the thermal properties of phonons in two-dimensional lattices. We measure the thermal conductivity and the specific heat capacity down to cryogenic temperature. The phonon transport crossovers from the diffusive to the ballistic regime when lowering the temperature below ~ 100 K. The temperature dependence of the specific heat capacity approaches a quadratic dependence, the signature of two-dimensional lattices. Both the thermal conductivity and the specific heat capacity measurements are consistent with predictions based on first-principles. Our result establishes a new strategy to investigate thermal transport in two-dimensional materials, and allows for exploring the phonon hydrodynamic regime, the anomalous heat conduction, and the phase transitions of electronic many-body collective phenomena in monolayers.

Abstracto

Los dicalcogenuros de metal de transición (TMD) monocapa suspendidos combinan una masa ultrabaja y propiedades ópticas excepcionales, lo que los convierte en materiales intrigantes para aplicaciones opto-mecánicas. Sin embargo, el bajo factor de calidad Q medido en los resonadores de TMD ha sido un obstáculo hasta ahora. En esta tesis, primero mostramos una lectura óptica ultra sensible de resonadores TMD de monocapa que nos permite revelar sus propiedades mecánicas a temperaturas criogénicas. Encontramos que el factor de calidad de los resonadores WSe_2 monocapa aumenta considerablemente por debajo de la temperatura ambiente, alcanzando valores tan altos como 1.6×10^4 en temperatura de nitrógeno líquido y 4.7×10^4 en temperatura de helio líquido. Esto supera el factor de calidad de los resonadores de grafeno monocapa con áreas de superficie similares. Al enfriar el resonador, la frecuencia de resonancia aumenta significativamente debido a la contracción térmica la red del cristal de WSe_2. Estas mediciones nos permiten estudiar experimentalmente el coeficiente de expansión térmica de las monocapas de WSe_2 por primera vez. Los altos factores Q también se encuentran en los resonadores basados en las monocapas de MoS_2 y $MoSe_2$. El alto factor de calidad que se encuentra en este trabajo abre nuevas posibilidades para acoplar estados vibracionales mecánicos a excitones bidimensionales, valley pseudo-spins y emisores cuánticos únicos y para experimentos opto-mecánicos cuánticos basados en la interacción de Casimir.

Las capacidades de detección ofrecidas por este nano-resonador mecánico de alto factor Q también son interesantes para estudiar propiedades termodinámicas en regímenes de la materia condensada a los que es difícil acceder. En la segunda parte de la tesis, utilizamos sistemas optomecánicos basados en una monocapa de $MoSe_2$ para probar las propiedades térmicas de los fonones en redes de cristales bidimensionales. Medimos la conductividad térmica y la capacidad calorífica específica hasta temperaturas criogénicas. Los régimenes de transporte de fonones pasan de el difuso al balístico al bajar la temperatura por debajo de $\sim$ 100 K. La dependencia de la temperatura de la capacidad calorífica específica se aproxima a una dependencia cuadrática, lo cual es la firma de las redes bidimensionales. Tanto la conductividad térmica como las mediciones de la capacidad calorífica específica son coherentes con las predicciones basadas en primeros principios. Nuestro resultado establece una nueva estrategia para investigar el transporte térmico en materiales bidimensionales y permite explorar el régimen hidrodinámico de fonones, la conducción de calor anómala y las transiciones de fase de los fenómenos colectivos de cuerpos electrónicos en monocapas.

Acknowledgements

First of all, I have to thank my supervisor Adrian Bachtold for giving me the opportunity to work in such a competitive research group and for successfully guiding me trough the process of my thesis. I also have to thank all the people that directly worked on this project. Starting by Antoine Reserbat-Plantey who was my mentor at the beginning of my PhD and patiently introduced me to all the technical and theoretical background needed to develop the research presented here. To Ioannis Tsiutsios who worked with me at the very beginning and was also a big part of my mentorship. Finally, to Slaven Tepšić who joined the team at the end of my PhD and brought a lot of motivation, curiosity and knowledge that pushed me to keep learning and advance in our research.

I have to thank to all the people that has collaborated in the research presented in the thesis: Kevin Shädler who introduced me into the exfoliation and transfer technique of 2D materials; Andrea Cepellotti, Francesco Mauri and Andreas Isacsson who developed the theory calculations and kindly shared their knowledge of the thermal transport of 2D materials work presented on the thesis; The team at INSA (Toulouse) that hosted me for a week to do absorption measurments, specially Xavier Marie who helped us with his broad knowledge in the optical properties of TMD materials and Marco Manca who performed the absorption measurements in our devices; Itai Epstein who performed very useful simulations to understand the laser interference in our setup; Francois Dubin who helped the team with his technical and fundamental knowledge in optics when I joined the team; Frank Koppens who brought interesting discussions on the optical and electronic properties of 2D materials.

I enjoyed all the years I spent in this research group thanks to the nice people I shared it with: Peter Weber, Jil Schweinder, Sergio de Bonis, Joel Moser, Johannes Güttinger, Jorge Vergara, Adrien Nouri, Simon Hurand, Carles Urgell, Wei Yang, Chandan Samanta and Gernot Gruber. Also to Prof. Pierre Verlot and Daiky Hatanaka that were hosted in our group and with which we had great discussions. I have to specially thank Alexandros Tavernarakis who patiently helped me to understand most of the basic concepts I know in optomechanics.

Contents

Chapter 1

Introduction

1.1 Transition metal dichalcogenides

In the last years a lot of focus and effort from the research and technology communities has been put into the investigation of two dimensional materials. This research wave was triggered by the discovery in 2004 of the first purely 2D lattice ever observed in nature, graphene. Graphene also proved to be the strongest material in the world and one of the best conductors of both electricity and heat. For these reasons its discovery was awarded with the Nobel prize in 2010. Since then, many other families of two dimensional materials have been isolated from its 3D form. These include transition metal dichalcogenides monolayers (SL TMDs). In contrast to graphene which is a zero bandgap semiconductor also referred as semi-metal, TMDs are direct bandgap semiconductors, which makes them particularly interesting for photo-detectors and light emitting devices. On top of that they exhibit physical properties that make them suitable for a wide number of other applications. For instance, the adsorption coefficient can be as high as 20%, a remarkable value considering that the material is atomically thick. In addition, TMD monolayers feature strong spin-orbit interaction, so that the valley degree-of-liberty of this material can be manipulated with the polarization of incident light. All these intrinsic properties of SL TMDs open many possibilities for photonics and spintronics applications.

1.2 Nano-mechanical systems

Mechanical systems are widely used for the detection of forces, accelerations and masses. Some of the most known devices are the atomic force microscope, the accelerometers present in cars and mobile phones, and mass spectrometers. On the fundamental research side, in 2000 the group of Andrew N. Cleland cooled the vibrational mode of a macroscopical resonator to its quantum ground state. In the last year mechanical oscillators (free standing mirrors) placed as the extreme of a Michelson interferometer were used in order to detect for the first

time a gravitational wave. For all these reasons, the study of mechanical oscillators is still a very rich research topic involving many companies and research groups around the world.

The fabrication of micro and nano-electro mechanical oscillators (MEMS and NEMS) can be done following a top-down or a bottom-up approach. In the top-down approach a bulk material is downsized and shaped into a resonator using well known techniques such as lithography and etching. In the bottom-up approach the fabrication of NEMS is based on nano-scale materials such as carbon nanotubes, graphene and other 2D materials. The top-down approach has the advantage of being more controllable, reproducible and scalable but there is a limit on how much their size can be reduced until surface defects of the material start to degrade their performance. In the bottom-up approach the control and the scalability of the fabrication is lower but the material defects are lower, allowing to study the fundamental aspects of a pristine nano-material.

1.3 Thermal transport at the nano-scale

The miniaturization of electrical circuits is key to the improvement of the performance of electronic devices. Specially, in the last years thanks to the appearance of nanomaterials. But the miniaturization of circuits is facing a major bottleneck. the heat generated by computing is poorly evacuated, so that the temperature of the circuit increases to extreme levels. Detrimentally, the operation speed of actual circuits gets limited by this heat bottleneck. This makes the study of heat transport at the nanoscale crucial for electronic device applications.

There are also fundamental aspects of heat transport that are exciting to investigate. There is a fundamental limit in how well heat can be transported. The limit is given by the quantum thermal conductance. Heat transport, and more specifically the specific heat, are a powerful tool to study phase transitions. This is particularly interesting for the study of electronic many-body collective phenomena in monolayers, such as the charge density wave order and unconventional superconductivity. Moreover, there's an interesting regime of thermal transport called hydrodynamic regime, which is specially robust in 2D layers and has not been measured so far. In this regime the heat is transported by collective excitations of phonons that can give rise to the second sound at relatively high temperatures.

Chapter 2

Nanomechanics and Optomechanics

2.1 Basics of nanomechanics

In this thesis we use the mechanical vibrations of a resonator based on a two dimensional semiconductor membrane (TMD monolyer) as a probe to investigate its material properties. The vast majority of the results of this thesis can be explained by the basic photothermal optomechanic linear oscillator driven by a coherent force. In this section we introduce the basic theory of nanomechanical oscillators in the linear regime.

2.1.1 The linear driven oscillator

The equation of motion that describes an undriven linear oscillator is the Hooke's Law.

$$m_{\text{eff}} \frac{d^2 z(t)}{dt^2} = -k \cdot z(t)\,, \tag{2.1}$$

here m_{eff} is the oscillator effective mass and k is the spring constant of the oscillator restoring force. The oscillator spring constant depends on material properties such as the geometry or rigidity and defines its natural vibration frequency $\omega_0 = \sqrt{\frac{k}{m_{\text{eff}}}}$. In most of the experimental results of this thesis we will use $f_0 = \omega_0/2\pi$ in Hz units.

In order to account for the forces exerted from the environment onto the resonator we add a friction-like term to 2.1 that is proportional to the velocity and the mass. Then we use $k = \omega_0^2 m_{\text{eff}}$ and divide the whole equation by m_{eff} to get

$$\frac{d^2 z(t)}{dt^2} + \Gamma \frac{dz(t)}{dt} + \omega_0^2 z(t) = 0, \tag{2.2}$$

here the Γ factor is the rate at which the oscillator exchanges energy with the environment. The Q-factor Q of a resonator is a quantity that stands for how much energy per cycle remains in the resonator.

$$Q = 2\pi \cdot \frac{\textit{Total Energy}}{\textit{Energy loss per cycle}}. \tag{2.3}$$

A good resonator that doesn't loose much energy via the friction (damping) term has $\Gamma \ll \omega_0$ and then the quality factor becomes $Q = \frac{f_0}{\Gamma}$. This is the case for the resonators described in this work.

The linear coherently driven oscillator

In the presence of a coherent driving force of the form

$$F(t) = F_0 cos(\omega t + \phi), \tag{2.4}$$

one can take 2.4 as the real part of

$$F(t) = F_0 e^{i(\omega t+\phi)}, \tag{2.5}$$

where ω and ϕ are the frequency and the phase of the driving force respectively. Defining $\hat{F} = F_0 e^{i\phi}$ and adding it to 2.2 we get

$$\frac{d^2z(t)}{dt^2} + \Gamma\frac{dz(t)}{dt} + \omega_0^2 z(\,t) = \frac{\hat{F}e^{i\omega t}}{m_{\text{eff}}}. \tag{2.6}$$

Assuming a solution of the form $z(t) = \hat{z}e^{i\omega t} = z_0 e^{i(\omega t+\Delta)}$ and plugging it in this equation we get

$$\hat{z}(\omega) = \frac{1}{m_{\text{eff}}(\omega_0^2 - \omega^2 - i\Gamma\omega)}\hat{F} = \hat{\chi}(\omega)\hat{F}(\omega), \tag{2.7}$$

where $\hat{\chi}(\omega)$ is the mechanical susceptibility, as a function of the force frequency. Then we express $\hat{\chi}(\omega)$ as $\chi(\omega)e^{i\varphi}$ and we have

$$\hat{z}(\omega) = \chi(\omega)e^{i\varphi}F_0 e^{i\phi}. \tag{2.8}$$

From this relation we can extract the resonator amplitude $z(\omega)$ and the phase difference between the force and the oscillators amplitude $\varphi(\omega)$ are

$$z(\omega) = \frac{F_0}{m_{\text{eff}}\sqrt{\left[(\omega_0^2 - \omega^2)^2 + \Gamma^2\omega^2\right]}}, \tag{2.9}$$

$$\varphi(\omega) = \arctan\left(\frac{-\Gamma\omega}{(\omega_0^2 - \omega^2)}\right). \tag{2.10}$$

Figure 2.1 shows 2.9 and 2.10 in the frequency domain. In the figure it is shown how the damping can be extracted from the width of the peak at one half of the maximum squared amplitude (FWHM). This is the way the damping will be extracted in order to calculate the mechanical Q factor in the rest of this work.

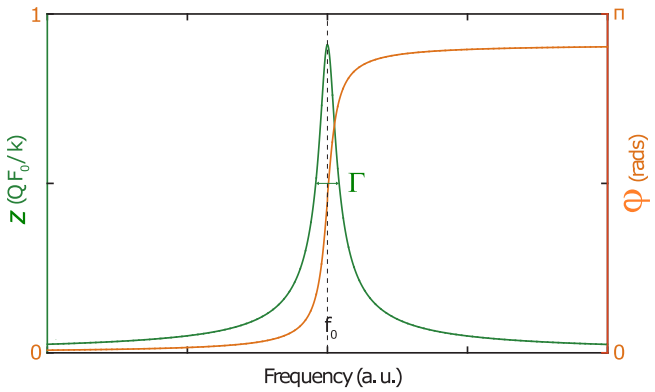

FIGURE 2.1: Plot of the amplitude response (green curve and left axis) and the phase response of an oscillator (yellow curve and right axis) as a function of the driving frequency. Adapted from [1]

The linear incoherently driven oscillator

When the resonator is driven by an incoherent force $\delta F(t)$ such as the one exerted by the fluctuating thermal forces, one can write the equation 2.6 as follows

$$\frac{d^2z(t)}{dt^2} + \Gamma\frac{dz(t)}{dt} + \omega_0^2 z(t) = \frac{\delta F(t)}{m_{\text{eff}}}. \tag{2.11}$$

Solving again the differential equation in the same way as for the coherently driven oscillator, we similarly obtain that

$$\hat{z}(\omega) = \hat{\chi}(\omega)\delta\hat{F}(\omega). \tag{2.12}$$

But in this case a different strategy is followed in order to experimentally extract information from the resonators response. What is measured is the power spectral density (PSD), which is the Fourier transform of the correlation function $C_x(\tau)$ of a time evolving signal $x(t)$. The PSD $S_x(\omega)$ is then

$$S_x(\omega) = \int_{-\infty}^{\infty} C_x(\tau)e^{i\omega\tau}d\tau, \tag{2.13}$$

with

$$C_x(\tau) = \langle x(t)x(t-\tau)\rangle, \tag{2.14}$$

where the time series $x(t)$ is measured in a time window ($-T \leq t \geq T$), so the correlation function is

$$C_x(\tau) = \frac{1}{2T}\int_{-T}^{T} x(t)x(t+\tau)dt. \tag{2.15}$$

If we do the Fourier transform of the correlation function we obtain that

$$F[C_x(\tau)](\omega) = \frac{1}{2T}\hat{x}(\omega)\hat{x}(-\omega) = \frac{1}{2T}|\hat{x}(\omega)|^2. \tag{2.16}$$

And therefore because of the definition of the PSD given before, we get

$$\frac{1}{2T}|\hat{x}(\omega)|^2 = S_x(\omega). \tag{2.17}$$

Then we write the equation 2.12 as

$$|\hat{z}(\omega)|^2 = |\hat{\chi}(\omega)|^2|\delta\hat{F}(\omega)|^2, \tag{2.18}$$

which means that

$$S_z(\omega) = |\chi(\omega)|^2 S_F(\omega). \tag{2.19}$$

It can finally be shown that the area under the one sided power spectral density is related to the root mean square of the displacement fluctuations $A = \frac{1}{2\pi}\int_0^\infty S_z(\omega)d\omega = x_{\text{rms}}^2$, where we use $x_{\text{rms}}^2 = \langle x^2\rangle$. Therefore A is related to the temperature T of the vibrating mode by the fluctuation dissipation theorem.

$$\frac{1}{2}m_{\text{eff}}\omega_0^2 x_{\text{rms}}^2 = \frac{1}{2}K_B T, \tag{2.20}$$

where K_B is the Boltzmann constant. This way, by measuring $S_x(\omega)$ we can get access to the temperature of the mode. Moreover, this equations shows that, the lower the resonators mass, the bigger it's displacement will be under the actuation of a thermal force.

2.1.2 TMD resonator as a capacitor circular plate

The mechanical resonators measured in this thesis can be described as circular membranes suspended over a trench at the bottom of which there's a metallic back gate [2, 3]. When they are electrically connected, the membrane and the gate form a capacitor. If a potential difference

V_g is applied between the membrane and the gate the flexible membrane gets pulled towards the bottom gate. This capacitive force F_{el} can be written as

$$F_{el} = \frac{1}{2}\frac{dC}{dz}(V_g + \Delta\phi)^2, \tag{2.21}$$

here $\Delta\phi$ is the work function difference between the TMD membrane and the metal top electrode. This force can be either a static force or an oscillating force by respectively applying a static voltage difference V_g^{DC} or an oscillating voltage difference $V_g^{AC}(f)$. The later can be used to drive the mechanical resonator when the frequency of the oscillating voltage is around the resonator natural frequency. When $V_g^{AC} \ll V_g^{DC}$ the driving force can be written as

$$F_{el}(f) = \frac{1}{2}\frac{dC}{dz}(V_g^{DC} + V_g^{AC}(f) + \Delta\phi)^2 \simeq \frac{dC}{dz}V_g^{DC}V_g^{AC}(f). \tag{2.22}$$

This force is used to drive our mechanical resonators in resonance for this thesis. Moreover, when V_g^{DC} is applied, there's a deformation of the membrane. We assume that the membrane is well clamped along its circular edge. The deformation generates a mechanical tension within the membrane and therefore a change of the resonance frequency. The variation of the resonance frequency due to the electrostatically applied pressure can be described by the following equation for membranes under initial strain (which will be the case for the devices presented in this thesis)

$$f_0 = \frac{1}{2\pi}\sqrt{\frac{4.92E_{2D}}{m_{eff}}\epsilon - \frac{\varepsilon_0}{d^3}\frac{0.271\pi R_0^2}{m_{eff}}(V_g^{DC} + \Delta\phi)^2}, \tag{2.23}$$

where E_{2D} is the two dimensional young modulus of the membrane, ε_0 is the vacuum permitivity and $d = \frac{d_{air}}{\epsilon_0} + \frac{d_{SiO_2}}{\epsilon_{SiO_2}}$ is the effective distance between the capacitor plates taking into acount the refractive index of the different dielectric materials (air and SiO_2 in our case). Finally, ϵ is the strain, defined as the ratio between the the actual radius and the initial radius of the resonator $\epsilon = \frac{R_0 - R_i}{R_i}$ being R_i the initial radius when there is no strain. One can see that when there's no effective gate voltage applied ($\Delta V_g^{DC} = V_g^{AC} + \Delta\phi = 0$) the natural resonance frequency is given by the first term of the equation which depends only on the tension, the young modulus and the effective mass. Due to thermal expansion the strain can change according to the following expression

$$\varepsilon = \varepsilon_0 + \int_{T=300K}^{T} \alpha(T_0)\mathrm{d}T, \tag{2.24}$$

were α is the thermal expansion coefficient. Therefore, a temperature change in the lattice of the TMD membrane is related to a resonance frequency shift.

The quality factor of the resonator is also affected by the static voltage applied between the membrane and the gate electrode. The mechanical motion generates a displacement current in the membrane and, thus, Joule heating.. This heating induces additional dissipation $\Gamma_J = Q^{-1}$ into the resonator and therefore it reduces its Q by an amount given by the expression

$$\Gamma_J = R_{el} C_z'^2 \frac{(V_g^{DC} + \Delta\phi)^2}{2\pi f_m m_{eff}}, \tag{2.25}$$

where R_{el} is the effective electrical resistance of the monolayer drum, C_z' is the derivative of the capacitance in the displacement direction and f_m is the measured resonance frequency [4].

2.2 Optomechanics

Optomechanics is the study of mechanical systems coupled to light. More particularly we will describe mechanical oscillators coupled to a laser beam via photothermal back action effects [5–9]. Back action stands for the effect of the measurement probe on the measured system. We use a laser that is used to measure the mechanical vibrations. The laser induces absorption heating in on the TMD membrane lattice which changes the resonant frequency and the damping of the resonator This back action has two origins, as discussed next.

2.2.1 Static photothermal back action

The most straightforward case is the static photothermal back action. When the TMD membrane is inside a laser field it will absorb a fraction of the power. This increases the temperature and causes the lattice to expand or contract changing the in plane tension of the resonator, and as seen in equation 2.23, which causes a shift of the resonance frequency. Moreover, the temperature change also affects the damping of the resonator (it will be shown in Chapter 5 that Γ is temperature dependent in TMD monolayers). For low enough powers, these effects are both linear with respect to the absorbed laser power. This means that the increase in temperature due to laser heating is less than 1 K. Therefore, one can write the resonance frequency and the damping as

$$f_m(P_{abs}) = f_m(P_{abs} = 0) + aP_{abs}, \tag{2.26}$$
$$\Gamma_m(P_{abs}) = \Gamma_m(P_{abs} = 0) + bP_{abs}, \tag{2.27}$$

where f_m is the measured resonance frequency, Γ_m is the measured damping and P_{abs} is the fraction of the input power that is absorbed in the monolayer TMD lattice.

2.2.2 Dynamical photothermal back action

The second type of back action is the dynamical back action. It is based on the same heating effect described above, but it takes into account the time scale at which the heating process happens and the fact that the amount of heating depends on the position of the membrane (given that the laser forms an interference pattern and therefore a gradient of intensity near the membrane). The equation of motion of a mechanical oscillator under a delayed optical force produced by an intensity gradient can be written as

$$\frac{d^2z(t)}{dt^2} + \Gamma\frac{dz(t)}{dt} + \omega_0^2 z(t) = \frac{1}{m_{\text{eff}}}\int_0^t \frac{dF_z[z(t')]}{dt}h(t-t')\mathrm{d}t', \quad (2.28)$$

here the term $h(t-t')$ takes into account the delayed response of the photothermal force. The time response is assumed to be an exponential decay of the form $h(t) = 1 - \exp(-t/\tau)$ where τ is the characteristic time for the heat to thermalise.

To get an intuitive picture, the absorption heating expands the TMD crystal, which is equivalent to a force. The displacement dependence of the absorbed power laser is not constant because of the interference pattern of the laser intensity in the direction perpendicular to the substrate. In the course of one period of the displacement oscillation, the absorbed laser power oscillates as well. Because the membrane takes a finite time to heat up or to cool down, the photothermal force oscillates with a finite phase shift compared to the displacement oscillation. The in-phase photothermal force modifies the resonant frequency by Δf_B and the out-of-phase photothermal force modifies the damping rate by $\Delta\Gamma_B$. Solving equation 2.28 we get that

$$\Delta(f_B)^2 = f_m^2\frac{dF}{dz}\frac{1}{k}\frac{1}{1+(2\pi f_m)^2\tau^2}, \quad (2.29)$$

$$\Delta\Gamma_B = -\Delta\Gamma_m Q\frac{dF}{dz}\frac{1}{k}\frac{2\pi f_m\tau}{1+(2\pi f_m)^2\tau^2}, \quad (2.30)$$

with $\frac{dF}{dt} \propto P_{abs}$ and $Q = \frac{f_m}{\Gamma_m}$. We can see that by quantifying the shifts of the frequency and damping due to the dynamical component of the back action, one can get the characteristic time constant of the back action force. Using equations 2.29 and 2.30 we get

$$\tau = \frac{\Delta\Gamma_B}{4\pi^2\Delta(f_B)^2} = \frac{\Delta\Gamma_B}{4\pi f_m\Delta f_B}. \quad (2.31)$$

This is the method that will be used in Chapter 6 to estimate the phonon thermalisation time of single layer transition metal dichalcogenides.

Chapter 3

Monolayer transition metal dichalcogenides

3.1 Crystal and band structure

Single layer (SL) transition metal dichalcogenides (TMDs) are a family of atomically thin direct bandgap semiconductors. They are of the form MX_2, they consist of one metal atom M (Mo, W, Nb...) and two chalcogenides X (S, Se, Te...). The structure of a single and bi-layer lattices and their respective unit cells are shown in figure 3.1a,b. The thickness t of a single layer, extracted from the layer-layer separation $c = 2t$ of bulk material, is about 0.6-0.65 nm. The bulk material consists of a number of single layers bound together by Van der Waals forces that are much weaker than the covalent forces that bound the atoms within a single layer. Therefore, single layers can be easily isolated using mechanical cleavage.

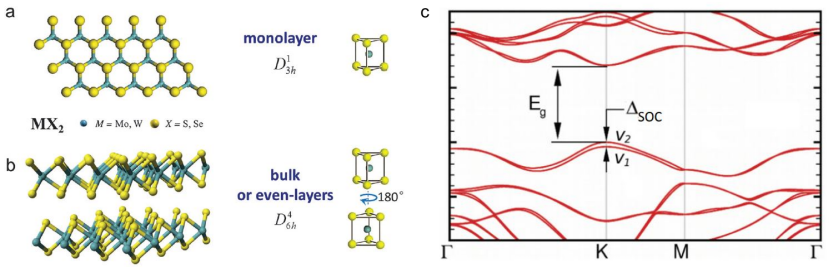

FIGURE 3.1: (a) and (b) show the lattice structure (left) and unit cell (right) of single-layer (top) and bi-layer (bottom) TMD crystal. (b) Calculated band structure of a MoX_2 TMD. It shows the valence band spin-orbit splitting Δ_{SOC} and the quasi particle band gap E_g. Adapted from [10] and [11]

The band structure of a typical SL TMD (Figure 3.1c) shows a direct band gap transition at the K point. The band gap energy depends on the TMD composition and ranges from 600 nm to 1500 nm [12]. SL

TMDs can be stacked on top of each other to make 2D heterostructures. This devices can take advantage of the strong absorption (or emission) of TMDs at different wavelengths. The absorption of TMDs is typically around 5-10% under white light illumination and can be as high as 20% when exciting an exciton resonance. All these properties make TMDs very attractive for applications in opto-electronic devices.

3.2 Optical properties

When a photon is absorbed by a TMD layer an electron-hole pair is created, this electron-hole quasiparticle is called exciton. Excitons in atomically thin TMDs have binding energies much larger than the ones in regular bulk semiconductors (up to 550 meV [13, 14]). This large binding energy originates from the confinement of electrons within the layer, so that the electric field outside the layer between the electron and the hole of excitons is poorly screened by other charges. Exciton resonances play an important role in the optical properties of single layer TMDs (fig. 3.2).

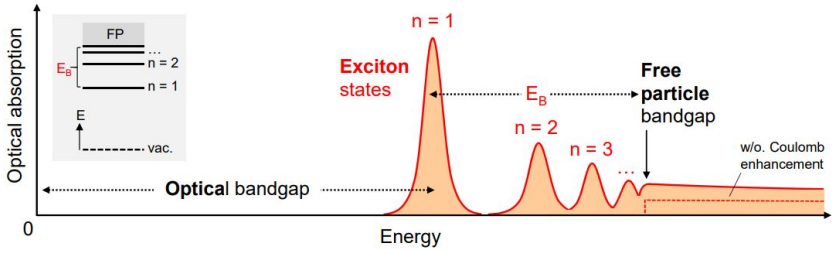

FIGURE 3.2: Ideal absorption spectrum of a single layer TMD. Adapted from [14]

Excitons are similar to the excited states of hydrogen atoms that can decay into a vacuum state by emitting a photon. This process is called photoluminescence. Analogously to the Hydrogen atom, they also present a series of excited states that get closer and closer at higher energies. These high energy excited states eventually merge with the free particle conduction band (Figure 3.2 inset).

3.2.1 Absorption

Excitons enhance the absorption in SL TMDs at given wavelengths. Figure 3.2 and figure 3.3a, show the ideal absorption spectrum and an experimental absorption measurement of a SL TMD, respectively. In order to investigate the absorption spectra of 2D materials there are several strategies (with the differential reflectance and the absorbance being the most commonly used). In the first one a white light or a laser

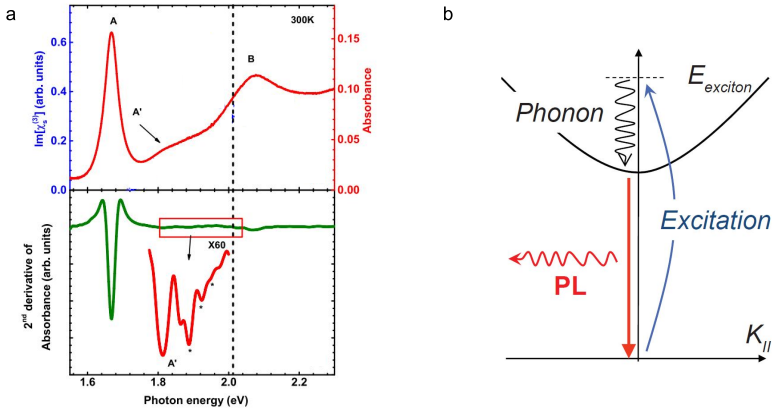

FIGURE 3.3: (a top) Linear absorption measured at room temperature on a WSe_2 monolayer. A and B corresponds to the exciton resonances from transitions from the two highest energy spin-orbit valance bands and the lowest energy conduction bands at the K(K') point of the Brillouin zone (see figure 3.1). A' denote the 2s state. (a bottom) Second-order derivative of the absorption spectrum. (b) Sketch of the phonon assisted photoluminescence process. (a) and (b) adapted from [15] and [1] respectively

is shined on the 2D material which is on top of a substrate. The reflected light is collected and sent to an spectrometer. The same process is repeated in a region of the substrate with no 2D material. By comparing (subtracting) the two measured spectra one gets the absorption at each wavelength. The first and second numerical derivative of the reflectance can be computed to get a more accurate information of narrow absorption features (Figure 3.3a). Alternatively, absorbance measurements can be carried out by shining light on the 2D material placed on a transparent substrate in this case. The spectrum of the transmitted light may be obtained, with the use of a spectrometer.

3.2.2 Photoluminiscence

In many semiconductors, photluminescence (PL) occurs when an electron is photo-excited from the valence band to the conduction band decays by emitting a photon. The energy of the photon corresponds to the energy of the band gap. However, when a photon is absorbed in a SL TMD, the electron and the hole bind together forming an exciton and then they recombine emitting a photon. The energy of the emitted photon in TMDs is lower that the energy of the band gap and corresponds to the energy of the exciton band. If the excitation energy is higher than the exciton energy, the photo-generated exciton will decay until it reaches the lowest level of the exciton band, and then it will recombine. The energy difference between the exciton emission

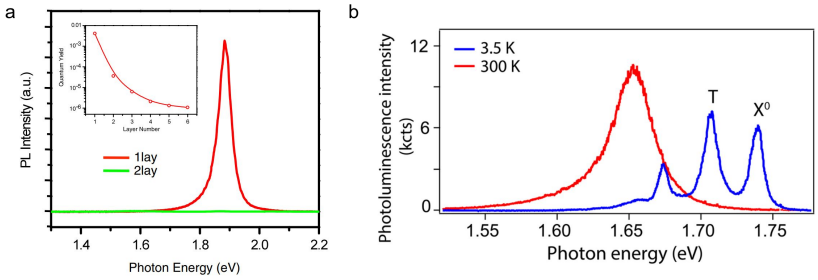

FIGURE 3.4: (a) Photoluminescence spectrum of a single layer (red) and bilayer (green) MoS_2. The inset of (a) shows the decrease of the photon quantum yield of the material from 1 to 6 layers. (b) Photoluminescence specra of a WSe_2 monolayer measured during this thesis at room temperature (red) and at 3.5K (blue). (a) Adapted from [16]

and the absorbed photon is mostly transferred to phonons. This process is called phonon assisted photoluminescence (Figure 3.3b). Out of resonance photoluminescence measurements consist on shining a laser (excitation laser at much higher energy than the exciton) on the sample and measuring the low-energy photons.

Due to interlayer interaction, when increasing the number of layers of the TMD the photoluminescence is reduced by several orders of magnitude (Figure 3.4a) [16]. At the same time by increasing the number of layers shifts the exciton energy. This makes PL measurments an easy way to determine if a TMD is single layer.

When lowering the temperature there are different effects in the photoluminescence. First, the inter atomic distance is reduced due to thermal expansion. This effect blue-shifts both the band gap and the exciton energies. Second, the thermal energy of the lattice and the carriers is reduced and this reduces the exciton-phonon interaction [17]. This effect reduces the broadening of the exciton peaks (Figure 3.4b). Therefore, the photoluminescence peaks get sharper and other exciton peaks such as the trion (exciton formed by two electrons and a hole or two holes and one electron) peak can be observed [18].

3.3 Mechanical properties

As seen in Ch. 2 (Eqs. 2.20 and 2.23), the mass of the resonator is a crucial parameter for sensing applications. A low mass provides a higher mechanical response to force noises and higher resonance frequencies, both increasing the resonator sensing capabilities, since the force noise is given by

$$S_{\mathrm{F}} = 4K_B T \frac{m_{\mathrm{eff}}}{Q}, \tag{3.1}$$

and the mass sensitivity is given by

$$S_{\mathrm{m}} = \frac{\delta f_{\mathrm{m}}}{m_{\mathrm{eff}} f_0}, \tag{3.2}$$

where f_{m} is the frequency of the oscillator after absorbing an aditional mass and f_0 is the initial frequency of the oscillator. The atomical thickness $t = 0.65$ nm (extracted from the $c = 2t$ lattice parameter and also measured by AFM) of the TMDs is one of the features that makes them very interesting for optomechanics. Here we will see that not only the mass but also the Young's modulus and the strain (equations 2.23 and 2.24) are important parameters in 2D optomechanical devices.

3.3.1 Young modulus

The two dimensional in-plane Young's modulus $E_{2\mathrm{D}}$ defines how a 2D material is susceptible to get strained ϵ when a stress σ is applied to it.

$$\sigma = E_{2\mathrm{D}}\epsilon. \tag{3.3}$$

In TMDs we have $E_{2\mathrm{D}\,\mathrm{WSe_2}}$=116 N·m^{-1} and $E_{2\mathrm{D}\,\mathrm{MoSe_2}}$=103.9 N·m^{-1} [19]. For comparison the Youngs modulus of graphene is $E_{2\mathrm{DGraphene}} =$ 340 N·m^{-1}. In addition to their great in-plane strength, TMDs can be strained up to ϵ=20% [20, 21].

3.3.2 Thermal expansion

For a two dimensional material, the thermal expansion coefficient α is defined as

$$\alpha(T) = \frac{1}{a(T)}\frac{da(T)}{dT}, \tag{3.4}$$

where $a(T)$ is the value of a given lattice parameter in equilibrium at a temperature T. In Fig. 3.5 the theoretically calculated thermal expansion coefficient of different TMD monolayers shows a strong dependence in temperature. Furthermore, in stark contrast to graphene and hexagonal boron nitride, TMDs present a positive thermal expansion coefficient [22, 23].

Due to their atomic thickness, the bending rigidity of 2D materials is small. Consequently, the resonance frequency of resonators based on this materials is dominated by tension. The resonance frequency is sensitive to the thermal expansion of the material.

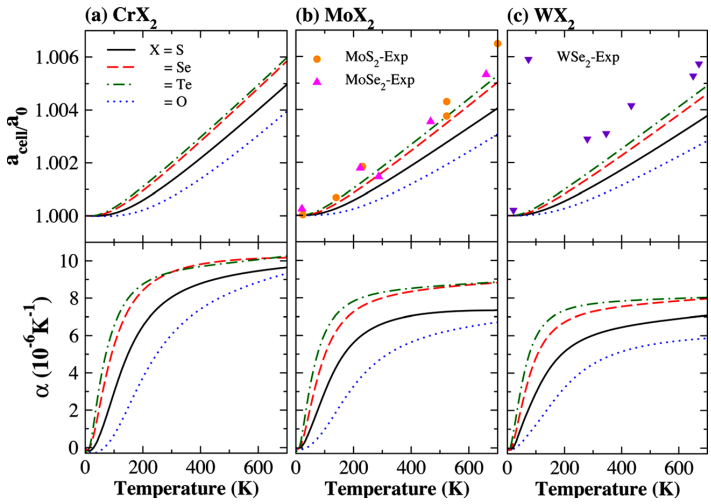

FIGURE 3.5: The upper panels correspond to the dependence of the in plane inter-atomic distance (lattice parameter) versus temperature and the lower panels show the temperature dependence of the thermal expansion coefficient. Adapted from [19]

3.4 Thermal transport

Thermal transport has been widely studied on microfabricated systems for over 20 years [24–27]. These systems have been used to understand the underlying nature of thermal energy transport in nanodevices microfabricated from bulk materials such as Si, SiC and SiN. Devices usually consist on suspended nanowires and suspended membranes of thicknesses of around one micron. The nanowires and membranes are connected to micro-engineered heat sources and thermometers that have to be carefully calibrated (Fig. 3.6). Using such systems the measurement of the quantum conductance of thermal transport was reported in 2000 [24] (Fig. 3.6a). The thermal transport in top-down microfabricated devices is rather well understood.

Thermal transport in individual nanoscale systems such as nanotube and graphene is rather challenging. New techniques were developed. This includes the Raman measurement of thermal transport in monolayers, where a laser beam is focused on a suspended monolayer [references]. The heat flow is given by the absorbed laser power, and the thermal gradient is measured from the shift in frequency of the Raman peak. This Raman measurement of thermal transport has been used by a large number of groups in the world [references]. However, such measurements cannot be carried down to helium temperature,

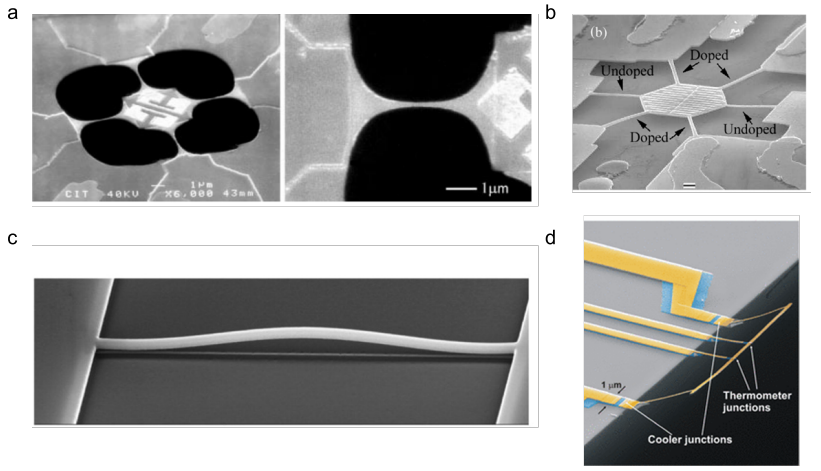

FIGURE 3.6: Collection of microfabricated devices used to study thermal transport of bulk materials such as Si, SiN, and SiC. Adapted from [24–27]

because large laser power is required to detect the temperature gradient. Beautiful experiments down to helium temperature were carried out by suspending either an individual carbon nanotube or an individual graphene flake between two microfabricated structures containing integrated heaters and thermometers [28–30] (Fig. 3.6). However, the fabrication of such devices is challenging, and the calibration of the measured thermal conductance has to be done in a careful way. Recently the heat transport of electrons in a graphene based bolometer was reported [31]. The measurement method consisted in probing the variation of the Jonson-Nyquist noise of a boron nitride/graphene/boron nitride suspended heterostructure coupled to a photonic cavity.

3.4.1 Thermal transport of 2D materials

Thermal transport in most two dimensional materials is carried out by phonons [32, 33]. There are different regimes of thermal transport. For instance, transport can be diffusive, ballistic or hydrodynamic [34]. Experimentally, one can probe the transition between different thermal transport regimes by measuring the thermal conductance K (resistance $1/K$) as a function of temperature [33, 34]. Other interesting quantities to measure are the phonon mean free path and the heat capacity. None of these quantities has been measured yet as a function of temperature in 2D materials.

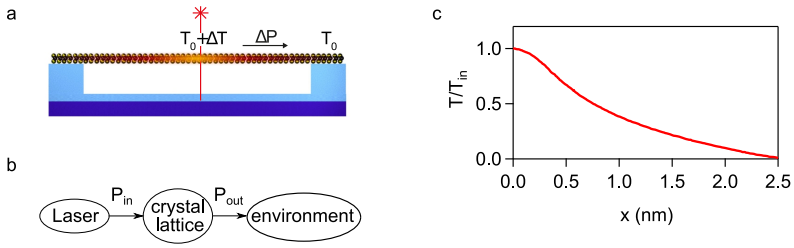

FIGURE 3.7: (a) Monolayer membrane coupled to a focused laser beam. The laser acts as a local heat source. The heat travels through the monolayer crystal from the center of the crystal to its circular clamping edge. Because of the thermal resistance, the heat flow ΔP leads to a temperature gradient ΔT. The yellow region corresponds to higher temperature, while red black regions correspond to lower temperature. (b) Schematic of the power flow. The power P_{in} flowing into the monolayer crystal is equal to the power P_{out} flowing out the crystal. (c) Normalized temperature profile in the radial direction of the TMD lattice calculated from equation 3.7 [35–42]

Thermal conductance

We can define the thermal conductance K as the power flow divided by the temperature gradient [35].

$$K = \frac{\Delta P}{\Delta T}. \tag{3.5}$$

Figure 3.7 depicts how a temperature gradient ΔT can be created by shining a laser onto the middle of a suspended TMD circular membrane. The heat flow ΔP given by the laser power absorbed in the membrane (Figure 3.7a). It is assumed that the absorbed energy is transferred to the phonons of the membrane (Figure 3.7b).

The thermal conductivity of graphene and other 2D materials has been intensively studied with Raman measurements [35–42]. The temperature at the center of the membrane is probed by measuring the shift of the Raman-peak frequency δf_{R} when sweeping the absorbed laser power P, which gives $\delta f_{\text{R}}/\delta P$. The temperature variation is calibrated by measuring the Raman-peak frequency as a function of the temperature of the setup, that is, $\delta f_{\text{R}}/\delta T$. The thermal conductance can be inferred from

$$K = \frac{\Delta P}{\Delta T} = \frac{\delta f_{\text{R}}/\delta T}{\delta f_{\text{R}}/\delta P}. \tag{3.6}$$

Many groups [35, 36, 40, 41] have successfully used this technique to measure the thermal conductivity of different 2D materials. However, due to the high power needed to excite Raman peaks (tipically about 100μW) this method can not be used at cryogenic temperatures.

Thermal conductivity

In order to compute the conductivity from the conductance, one has to take into account the thickness of the membrane and the Gaussian profile of the laser beam. We also assume that the circular clamping edge acts as a heat sink (which was confirmed experimentally by Yan and collaobrators *Yan et. al.*) [40].

The thermal conductivity κ is inferred from K using the heat diffusion equation as introduced by [41]. The spatial temperature rise (Figure 3.7b) induced by the absorbed laser power variation ΔP along the radial cordinate r is given by

$$\Delta T(r) = \frac{\Delta P}{2\pi\kappa t} \ln\left(\frac{R_0}{r}\right)\gamma(r), \tag{3.7}$$

where K is the effective conductance, t is the thickness of the TMD monolayer and R_0 is the radius of the suspended drum. Finally $\gamma(r)$ is given by

$$\gamma(r) = 1 + \frac{\mathrm{Ei}\left(-\frac{r^2}{r_0^2}\right) - \mathrm{Ei}\left(-\frac{R_0^2}{r_0^2}\right)}{2\ln\left(\frac{R_0}{r}\right)} \tag{3.8}$$

where Ei is the exponential integral function. The edge of the drumhead is assumed to be well thermalized to the environment, so that $T(R = R_0) = T_0$ (Figure 3.7a). The temperature decreases logarithmically along r between r_0 and R_0 as seen in Figure 3.7c. Then one gets the final expression

$$\kappa = K\frac{\eta}{2\pi t}, \tag{3.9}$$

here we get that η is a constant of the order of unity, which depends on the temperature profile along the radial coordinate r.

Chapter 4

Device Fabrication and Measurement Setup

4.1 Introduction

In this chapter we will address the details of the device fabrication and the measurement setup. The fabrication of all the devices studied in this work was fully performed at ICFO using the same process for all the samples. The nano-mechanical readout and the microphotoluminescence setup were both mainly developed by coworkers Antoine Reserbat and Ioannis Tsioutsios, also at ICFO.

4.2 Fabrication of single layer transition metal dichalcogenide nano-electro-mechanical system

All the devices measured in this thesis consist of drumhead resonators based on single layer TMDs. More specifically, the materials used are WSe_2 and $MoSe_2$.

4.2.1 Substrate: electrodes and holes patterning

The substrates on which the single layer flakes will be transferred are fabricated starting from Si^{++}/SiO_2 chips. The Si back gate tickness is 1 μm and the SiO_2 thickness is 285 nm. We evaporate gold electrodes and etch 3-5 μm holes in the SiO_2 using the following fabrication process (Fig. 4.1). First, a PMMA mask is used to pattern the 5 μm wide gold electrodes by electron beam lithography (EBL). Once the PMMA is patterned by EBL, we develop the PMMA using MIBK (4-methyl-2-pentanone), and we evaporate a 5 nm thick Titanium adhesion layer and a 50-100 nm thick gold layer, using a thermal evaporation system. The PMMA, together with the residual gold, is lifted-off using acetone. Once the gold electrodes are patterned we etch the holes in the SiO_2.

For this we again cover the chip with PMMA and then pattern the (3-5μm) structure by EBL. As for the electrodes, the pattern exposed to the electron beam is developed. Then, the exposed SiO_2 patterns are etched by Reactive Ion Etching (RIE). The trench depth used for most of the devices presented in this thesis ranges between 150 and 180 nm. The residual PMMA is finally removed by acetone and oxygen plasma cleaning.

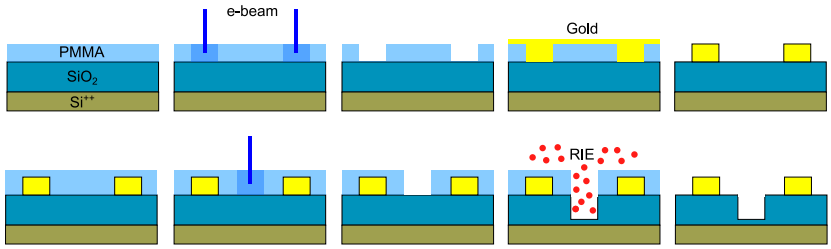

FIGURE 4.1: Sketch of the fabrication process.

4.2.2 Exfoliation

Single layer TMDs are obtained by mechanical exfoliation of bulk material. The starting bulk material are commercial crystals (Figure 4.2b.1, b.3) from hqgraphene and 2D semiconductors. This commercial bulk TMD crystals are produced by chemical vapor deposition (CVD). The mechanical exfoliation is done using a silicon based organic polymer called polydimethylsiloxane (PDMS). This polymer is widely used, because of the low amount of contamination that is left on the exfoliated flakes.

The exfoliation step is made on a thick (1-3 mm) PDMS home made layer which is stuck on top of a glass slide (figure 4.2a, b.4). This slide is used to hold the flake downwards during the transfer of the flake to the substrate (figure 4.2c). In order to identify single layer flakes we used reflectance optical contrast measurements (figure 4.2b.2). Single layers are confirmed afterwards with room temperature photoluminescence measurements.

4.2.3 Dry transfer and final device

In this process a micro-manipulator is used to position the flake on top of the substrate (Figure 4.2c). The glass slide (with the thick PDMS layer and the flake) is attached on the arm of a micro-manipulator. The substrate is fixed on a rotation stage. By keeping the substrate in focus, the flake is aligned with respect to the prepatterned structure. Once the PDMS carrying the flake is in contact with the substrate we

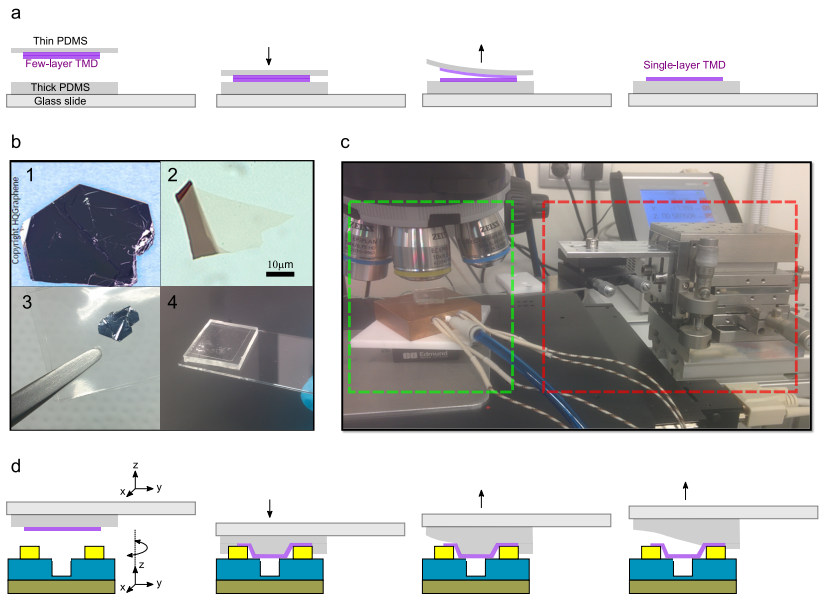

FIGURE 4.2: (a) Sketch of the exfoliation step. (b) Images of (b.1 and b.3) bulk WSe_2 and $MoSe_2$, (b.2) single layer exfoliated on top of a thick PDMS laayer as the one shown in (b.4), (b.4) a glass slide with a thick PDMS layer, with exfoliated few-layer flakes on top. (c) Picture of the transfer setup. The micromanipulator contolling the glass slide and the flake position is in the red dashed square. The optical microscope, the down facing glass slide and the substrate mounted on a rotation stage are in the green dashed sqare. (d) Sketch of the dry transfer process.

start to slowly pull off the PDMS, so that the flake is left behind on the substrate (figure 4.2d). This is process is very robust, with success yields of around 70-80% for holes of 3 μm. Figure 4.3 shows a collection of some of our devices fabricated with this technique. As discussed later, this fabrication process produces a fairly homogeneous and reproducible initial tension in the drums [43–46].

4.3 Experimental setup

Our measurement setup allows us to measure the mechanical vibrations of monolayer drums and to carry out photoluminescence measurements of TMD flakes. For all the measurements the sample is inside a cryo-free cryostat (3-300K) and under high vacuum ($10^{-6} - 10^{-8}$ mbar).

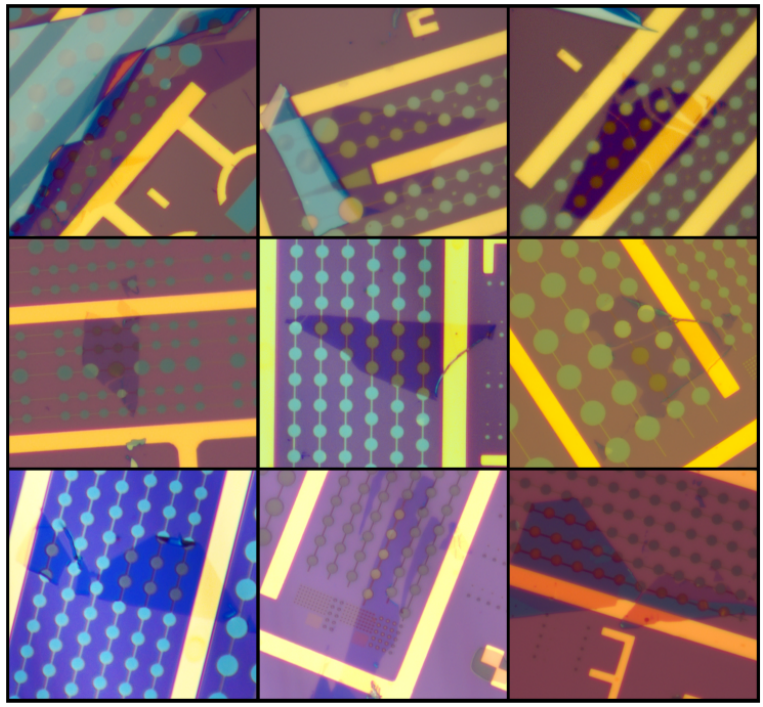

FIGURE 4.3: Optical images of fabricated devices. The first row shows single layer WSe_2 devices and the other are made of single layer $MoSe_2$.

4.3.1 Motion excitation and detection

The laser source is a continuous wave HeNe laser. The laser is focused on the sample by a MITUTOYO 100x objective with NA=0.7 and focal length f=200mm. The spot size (beam waist) of the laser beam has a radius r=350 nm. The focused light goes trough the suspended TMD, is reflected on the Si back gate and goes trough the flake again. The reflected light is sent to an avalanche photo-diode (Thorlabs APD130A/M) with a bandwith of 50 MHz.

The detection principle works as follows. The input and reflected beam interfere with each other creating an interference pattern. A simulation of the interference pattern is shown in figure 4.4c. Therefore the TMD membrane will vibrate in a gradient of intensity. Because the TMD membrane has a constant absorption coefficient (5-10% at $= 633nm$), it will absorb a different amount of light depending on its position. The vibrating membrane modulates the reflected intensity. The modulated reflection is then detected by the APD which feeds a signal analyzer (SA Agilent Technologies CXA N9000 9kHz-3GHz).

The cryostat contains radio-frequency connections that allow us to apply an AC voltage V_g^{AC} between the flake and the Si back gate. The

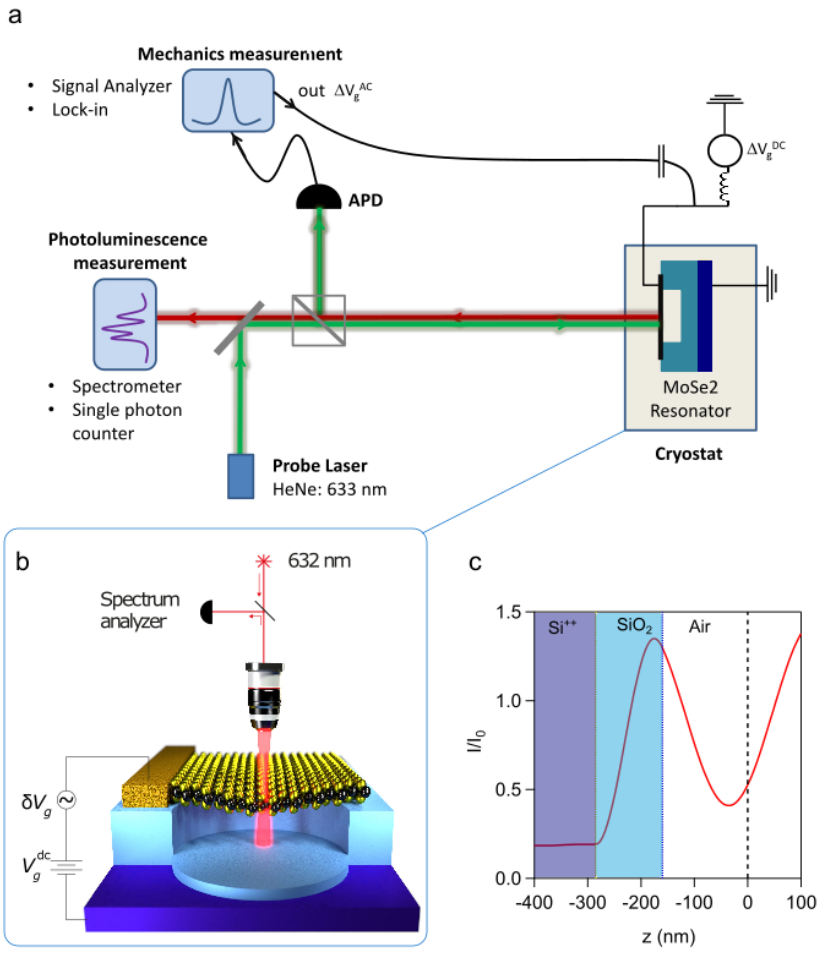

FIGURE 4.4: (a) Schematic of the full setup. The green line corresponds to the HeNe-633 nm probe laser used to probe the mechanics and excite the PL. The red line corresponds to the emitted photoluminescence. (b) Schematic of the device probed with the lase beam. (c) Numerical simulation of the intensity profile of the interference patter created by the reflected laser at the Si/SiO_2 interface. The blue region corresponds to the SiO_2 layer and the black dashed line corresponds to the position of the TMD for the sample discussed in Ch. 6.

signal of the vibrations is detected with a spectrum analyzer.

The setup has another excitation source, a titanium-sapphire laser (TiSa). The intensity of this laser can be modulated by an acousto-optical modulator (AOM) in order to photo-thermally actuate the membrane.

4.3.2 Photoluminescence

The setup allows us to measure the photoluminescence emission of the TMD flakes. We use a dichroic mirror that reflects the HeNe light but is transparent to higher wavelengths. This way, only the PL signal is transmitted trough this mirror. The PL signal is measured by a Single Photon Counter APD or a Spectrometer. The first one measures with very high efficiency the emitted photons, providing information about the PL intensity. The second one provides spectral information of the emitted photons.

Chapter 5

TMD Nano-resonators at Low Temperature

5.1 Introduction

The results of this chapter were published in [High Quality Factor Mechanical Resonators Based on WSe_2 Monolayer, *NanoLetters*, 16.8 (2016)]

Monolayer transition metal dichalcogenides (TMDs) are two-dimensional direct bandgap semiconductors that have attracted considerable attention because of their unique optical properties [16, 30, 47–56]. In principle, suspending such monolayer TMDs should form remarkable opto-mechanical resonators. They are extremely thin, like graphene [57–61]. Owing to their low mass, the mechanical vibrational states of TMD resonators are extremely sensitive to external force [62] and adsorbed mass [63]. This holds promise for sensing applications and for coupling mechanical vibrational states to various optical degrees of freedom of monolayer TMDs, such as bright and dark two dimensional excitons [16, 49], valley pseudo-spins,[30, 50, 53] and single quantum emitters embedded in the monolayer [48, 52, 55, 56]. However, semiconducting TMD mechanical resonators have been operated only at room temperature thus far [43, 64–67]. Room-temperature operation is detrimental to opto-mechanical experiments, because the recombination and coherence time of two-dimensional excitons and valley pseudospins are short, and single quantum emitters only emerge at cryogenic temperatures. An even greater obstacle for all these experiments is the low quality factor Q achieved so far in monolayer TMD mechanical resonators ($Q \leq 100$) [66–68]. Therefore, it is important to develop a method to measure TMD resonators at cryogenic temperature in order to reduce damping. Electrical mixing techniques have been used to measure nanotube, graphene resonators, and other metallic nanosystems at helium temperature [4, 58, 60, 61, 69, 70] but such techniques are challenging to apply to semiconducting TMD resonators without Joule heating because of their high electrical resistance. Here, we show that optical detection of TMD resonators can

be employed down to 3.5 K without being affected by laser heating. This is possible because we have found that the Q-factor becomes extremely high at low temperature, allowins us to detect mechanical vibrations with low laser power.

5.2 Device characterization

We produce drumhead nanoresonators based on WSe_2 monolayers. The fabrication relies on the dry transfer of thin WSe_2 crystals over prestructured holes. In this first section we characterize the basic features of the device. We start with photoluminescence characterization at room and low temperature, to quantify the number of layers and the doping level. We also test the mechanical vibrations of different devices and their mechanical response to the electrostatic actuation at different temperatures.

5.2.1 Photoluminescence

Regions corresponding to monolayers are identified by the enhanced emission in photoluminescence maps (as explained in Ch. 3) and the corresponding spectra (Fig. 5.1 b,d). At 3.5 K, these spectra feature narrow peaks associated with two-dimensional excitons and trions, labeled as X^0 and T, respectively. The observation of trions indicates that the monolayer is doped, which we attribute to molecules adsorbed on its surface.

5.2.2 Driven mechanical response

The mechanical vibrations are detected by optical interferometry [7, 57] using ultralow laser power down to 70 nW in order to prevent heating. A continuous wave laser impinges on the device, and the reflected laser light is modulated by an amount proportional to displacement of the resonator. More specifically, the laser forms a standing wave pattern in the direction perpendicular to the Si substrate, such that the displacement of the WSe_2 monolayer modifies its optical absorption [7, 57]. In order to prevent heating of the WSe_2 lattice, the laser power is kept as low as possible, and the reflected light is collected with a large numerical aperture objective and detected with an avalanche photodetector (APD).

We measure driven mechanical spectra such as those in Fig. 5.2. We also measure the shape of the mechanical eigenmode by measuring the driven displacement at different positions (Fig. 5.1 e).

Motion is actuated by applying an oscillating voltage between the monolayer and the back-gate of the substrate [57] that together form a capacitor. This capacitive actuation is possible because the monolayer is doped. Given the high quality factors of the resonators, the applied

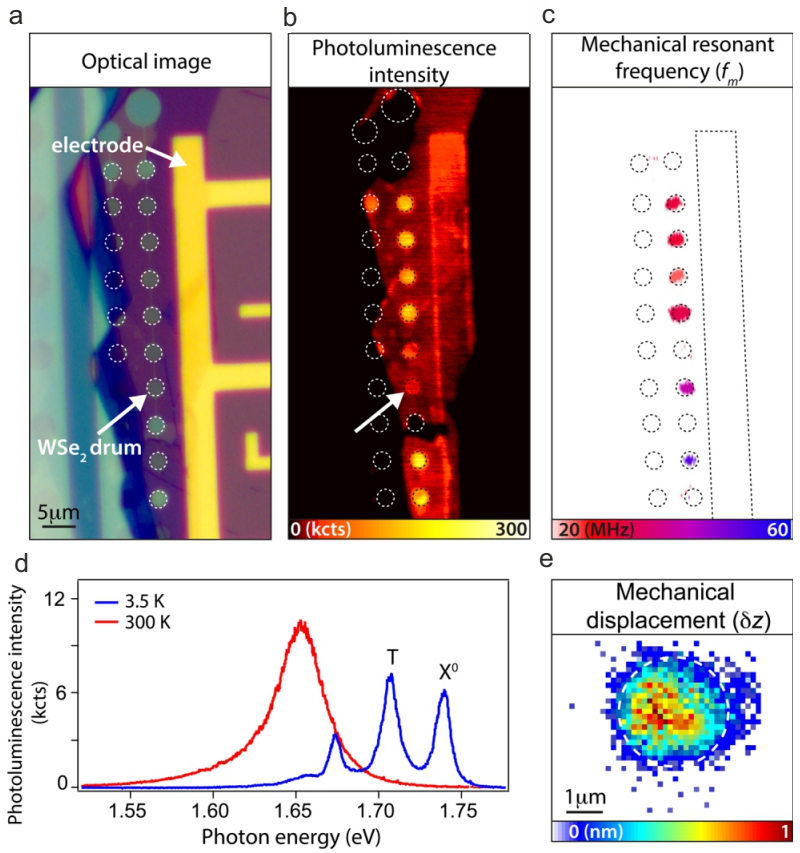

FIGURE 5.1: Optical image of an array of WSe_2 mechanical resonators. For the same device, both emission and a mechanical spectrum are recorded at each laser position, thus providing a spatial map of the WSe_2 PL emission (b), and the extracted mechanical resonance frequency f_m (c). For each position of the laser, we record the mechanical spectrum and we extract the resonance frequency of the fundamental mode. (d) Photoluminescence spectra of monolayer WSe_2 at 300 K (red) and 3.5 K (blue). (e) Spatial map of the nanomotion amplitude for a WSe_2 monolayer resonator with the drive amplitude V_g^{AC} = 1 mV. Dash line represents the WSe_2 resonator outline. The drum studied in (d,e) is marked by an arrow in (a,b).

driving force has to be low in order to keep the resonator amplitude in the linear regime. Measurements presented in this work are carried out in the linear regime; an example of nonlinear Duffing response is shown in Fig. 5.3.

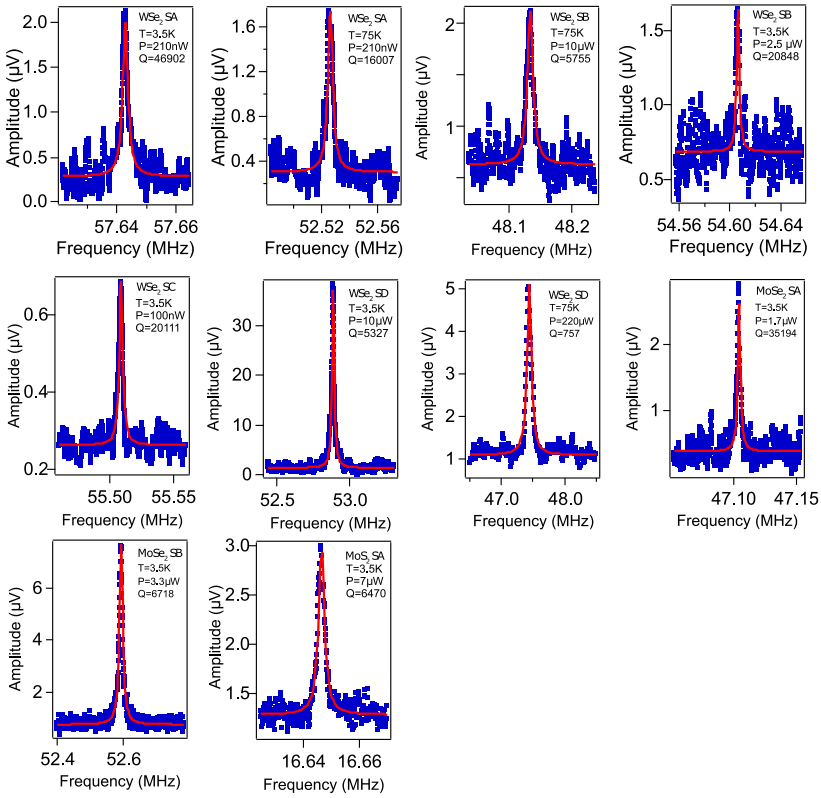

FIGURE 5.2: Driven spectra of different resonators based on WSe_2, $MoSe_2$ and MoS_2 monolayers. Sample number is undicated as SA, SB, SC and SD 5.11.

5.3 Mechanical damping

5.3.1 Damping as a function of temperature

The parameter that has the most dramatic effect on the damping is the temperature. Fig. 5.4b shows the temperature dependence of the Q-factor.

For the best resonator, we observe ultrahigh quality factors up to Q= $f_m/\Gamma_m \sim 47\,000$ at helium temperature, where f_m is the resonant frequency and Γ_m is the resonance line-width. This is more than 2 orders of magnitude higher than the Q-factor of monolayer TMD resonators previously measured [43, 67, 68]. This also surpasses by a factor 3 the highest measured Q-factor of graphene resonators with similar dimensions and cooled at helium-4 temperature [58, 61]. Upon increasing the cryostat temperature, the Q-factor decreases (Fig. 5.4b).

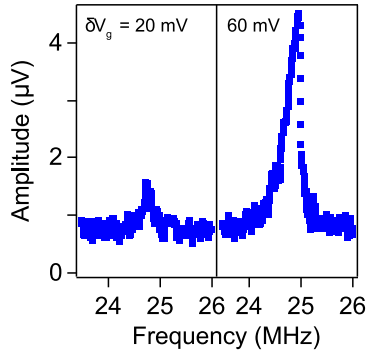

FIGURE 5.3: Response of a monolayer WSe_2 mechanical resonator to an oscillation force at 300K. The response is nonlinear at high drive voltage (right panel).

It reaches Q $\sim$ 166 at room temperature, a value consistent with previous reports.

5.3.2 Damping vs laser power

As explained in Chs. 2 and 3, the effect of the laser power and temperature are linked, since the absorbed laser power can heat the membrane lattice and induce forces on the resonator. For this reason, the low laser power used to detect the vibrations is central to achieving these ultrahigh Q-factors. Fig. 5.5 displays the quality factor as a function of the input laser power P. We find that the quality factor remains approximately constant for P below $\sim$200 nW. For larger P, the Q-factor decreases, indicating that the laser perturbs the dynamics of the resonator.

In the following, we show that the laser affects the resonator through two physical processes: absorption heating and dynamical photothermal back-action [5, 7]. In absorption heating, the laser increases the temperature of the device lattice, so that the damping Q^{-1} is expected to increase (as shown in Fig. 5.4b). Dynamical photothermal back-action arises from the gradient of the photothermal force and the finite response time of the resonator to a temperature change. The resulting delayed force modifies the damping of the resonator by $\Delta\Gamma = \Delta(Q^{-1})$ (Eq. 2.30) and, therefore, its effective temperature. Depending on the sign of the gradient $\frac{dF}{dz}$ (Eq. 2.30), $\Delta(Q^{-1})$ is positive and the resonator cools down, or $\Delta(Q^{-1})$ is negative and the resonator heats up.

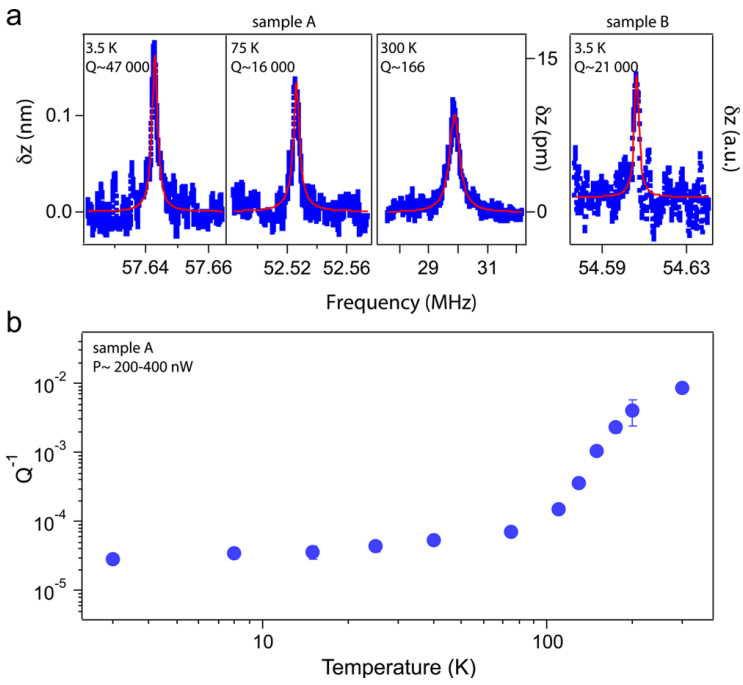

FIGURE 5.4: High Q-factor WSe_2 mechanical resonators. (a) Resonator displacement as a function of drive frequency for devices A (shown in Fig. 1d,e) and B. The solid red line is a Lorentzian fit to the data (blue points). We set ΔV_g^{AC} = 15 mV at 3.5 and 75 K and 100 mV at 300 K. (b) Mechanical damping (Q^{-1}) as a function of cryostat temperature. The data points below 110 K are taken with 200 nW laser power and 400 nW otherwise. We use ΔV_g^{AC} between 10 and 50 mV depending on the temperature.

Laser heating and dynamical back action

We measure the temperature of the mechanical mode by detecting the thermal vibrations of the resonator (Fig. 5.6a). The capacitive force is switched off, and the resulting displacement noise is recorded with a spectrum analyzer. Fig. 5.6a shows that upon increasing P, the integrated area of the thermal resonance and its line width get both larger with the cryostat temperature set at T_{cryo} = 20 K. This shows that the temperature T_{mode} of the mechanical mode and the damping Q^{-1} both increase, which is in agreement with the absorption heating process.

As explained in Ch. 2, Eq. 2.20 relates the area under the curve of the thermal motion spectrum of the resonator to its mode temperature. The thermal resonance area $\langle z^2 \rangle$ in the displacement spectrum allows to quantify T_{mode} using $m_{eff}\omega_m^2\langle z^2\rangle = k_B T$ mode with m_{eff} the effective mass of the mechanical mode and $\omega_m = 2\pi f_m$. Fig. 5.6b shows

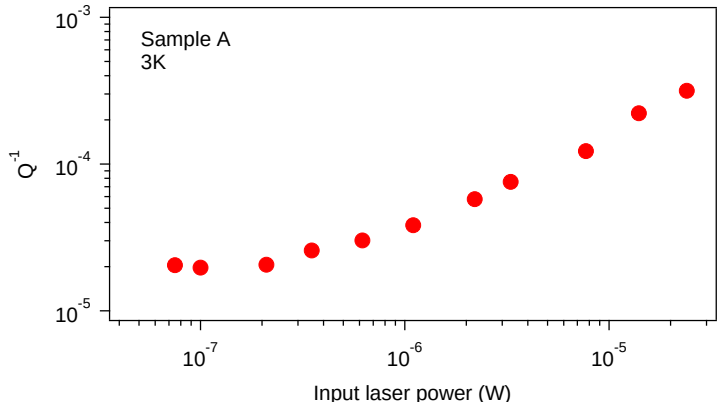

FIGURE 5.5: Mechanical damping (Q^{-1}) as a function of laser power

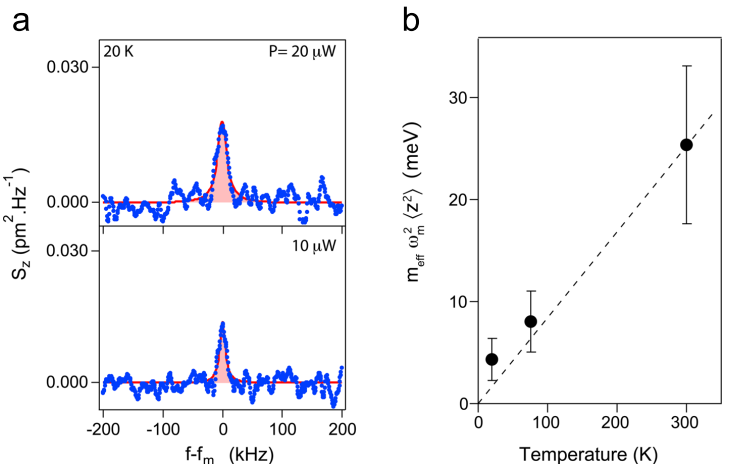

FIGURE 5.6: (a) Resonator displacement noise spectral density S_z taken at 20 K for different imput laser powers P. The area of the Lorentzian fit (red curve) corresponds to the displacement variance $\langle z^2 \rangle$. The increase of this area with P is a signature of laser-induced heating. (b) Energy of the resonator mode $m_{\text{eff}}\omega_{\text{m}}^2 \langle z^2 \rangle$ extracted from noise spectra as a function of the cryostat temperature. Dashed line corresponds to $m_{\text{eff}}\omega_{\text{m}}^2 \langle z^2 \rangle = k_B T$.

that T_{mode} scales roughly linearly with T_{cryo} at high temperature, indicating that the resonator thermalizes with the cryostat. However, the resonance area at T_{cryo} = 20 K corresponds to $T_{\text{mode}} \sim 50$ K, showing that absorption heating is substantial. The reason for this observed heating is the particularly large laser power needed to resolve thermal vibrations, that is, P > 10 μW.

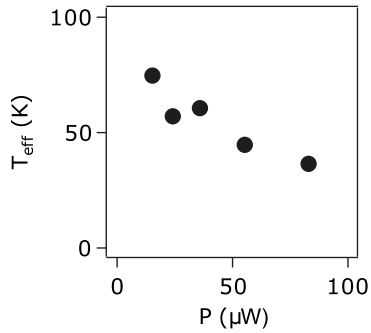

FIGURE 5.7: Effective temperature T_{eff} of the fundamental mechanical mode as a function of the laser probe power measured with the cryostat temperature set at 75 K. T_{eff} is extracted by fitting the thermal resonance in the noise spectrum, as described in the main text. As the laser power increases, the mechanical mode cools down through dynamical photothermal back-action.

We find that dynamical photothermal back-action also lowers the Q-factor. For temperature cryostat above 70 K, we find that the mechanical mode gets effectively colder upon increasing P (Fig. 5.7), indicating that dynamical photothermal cooling becomes more efficient than absorption heating. The dynamical photothermal cooling is related to the force gradient dF/dz induced by the standing wave of the laser in the direction perpendicular to the substrate, as shown in ref [7]. The cooling of the mode observed in our experiment indicates that $dF/dz > 0$ and $\Delta(Q^{-1}) > 0.31$ This confirms that the high Q-factors measured at low power in Figs. 5.4a and 5.2 do not originate from the narrowing of the mechanical linewidth due to dynamical photothermal back-action.

5.3.3 Damping as a function of DC back gate voltage

The high Q-factors of capacitively driven vibrations measured at low laser power are obtained upon tuning the back-gate voltage V_g^{DC} as close as possible to the equivalent work function difference $\Delta\phi$ between the monolayer and the back-gate (Fig. 5.8). Otherwise, the Q-factor can significantly decrease due to the electronic Joule dissipation of the displacement current through the monolayer, the current being generated by the TMD motion. As described in Ch. 2 the contribution of the Joule dissipation is

$$Q_J^{-1} = R_{el}\frac{C_z'^2(V_g^{DC} + \Delta\phi)^2}{2\pi f_m m_{eff}}, \tag{5.1}$$

where $C_z' = \frac{dC}{dz}$ is the derivative of the capacitance between the suspended monolayer and the back-gate with respect to the displacement, and R_{el} is an effective electrical resistance of the monolayer [4]. Our data are well described by $Q_{total}^{-1} = Q_{WSe_2}^{-1} + Q_J^{-1}$ where Q_{WSe_2} is the quality factor measured at $V_g^{DC} \approx \Delta\phi$ (Fig. 5.8b). The comparison between the measurements and eq 5.1 leads to R_{el} = 305 kΩ. Such a value is comparable to the sheet resistance of a TMD monolayer with weak doping [71, 72]. We emphasize that a direct comparison between R_{el} and the sheet resistance is nontrivial, because of the uncertainties in the geometry associated with R_{el}.

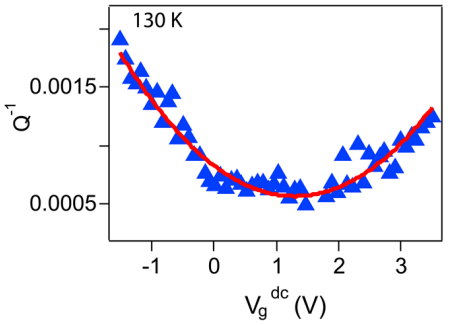

FIGURE 5.8: Mechanical damping Q^{-1} as a function of backgate voltage V_g^{DC}. The red line is a fit to eq 5.1. We use V_g^{AC} = 10 mV

5.4 Testing the thermal expansion coefficient

We now turn our attention to the temperature dependence of the resonant frequency, which is found to be particularly strong (Fig. 5.9a,b). This behavior is attributed to the thermal expansion of the membrane, which modifies the tensile strain ϵ of the suspended monolayer as explained in Ch. 2 using eqs. 2.23 and 2.24.

The presence of tensile strain is further supported by the convex parabola observed in the dependence of the resonant frequency on the static back-gate voltage (Fig. 5.10). The convex parabola, which has been observed in highly strained nanotube and graphene resonators [60], has an electrostatic origin. For a circular membrane under tensile stress, the resonant frequency is given by [3]

$$f_m = \frac{1}{2\pi}\sqrt{\frac{4.92E_{2D}}{m_{eff}}\epsilon - \frac{\varepsilon_0}{d^3}\frac{0.271\pi R_0^2}{m_{eff}}(V_g^{DC} + \Delta\phi)^2}, \tag{5.2}$$

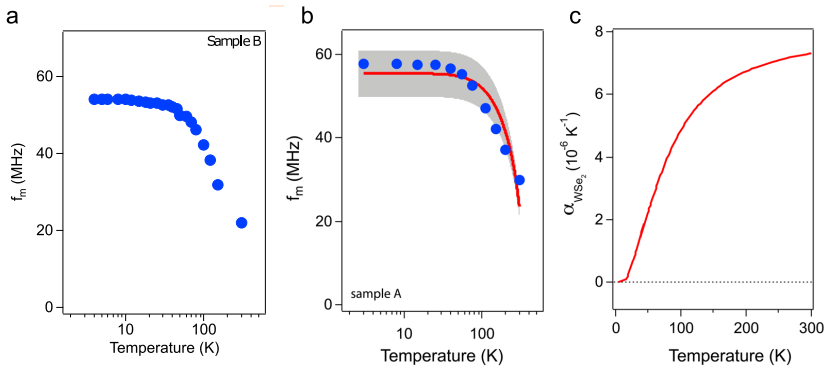

FIGURE 5.9: Mechanical resonant frequency f_m as a function of temperature for two different devices. We use V_g^{AC} between 10 and 50 mV depending on the temperature. Red curve in (b) is a fit to Eq. 5.2 with $V_g^{DC} = \Delta\phi$ and using the thermal expansion coefficient α of WSe_2 predicted in ref [19] and shown in (c). The gray area represents the imprecision due to the thermal expansion coefficient of the substrate.

here, E_{2D} = 116 N·m1 is the two-dimensional Young modulus of WSe_2 monolayer [19], R_0 =1.5μm is the drum radius, and d = 180 nm is the equivalent separation between the membrane and the backgate electrode (Ch. 2). The measurements can be well described by Eq. 5.2 using $m_{eff} = 3x10^{17}$ kg. The obtained mass is close to the value expected from the two-dimensional mass density ρ = 12 μg.m^2 of WSe_2, which gives $m_{eff} = 0.27\pi R_0\rho = 2.3x10^{-17}$ kg. This good agreement shows that the resonator mass predominantly consists of the WSe_2 lattice with only a small fraction of additional mass from adsorbed molecules.

Our measurements allow us to study the thermal expansion coefficient α_{WSe_2}, an important mechanical property of monolayer TMDs that has not been experimentally investigated thus far. That is, we use the thermal expansion coefficient $\alpha_{WSe_2}(T)$ calculated in the theory work in ref [19] in order to reproduce the measured temperature dependence of the resonance frequency. Fig. 5.10c shows that the calculated $\alpha_{WSe_2}(T)$ is positive, in stark contrast to the negative coefficient encountered in many two-dimensional layers, such as graphene [22, 58, 73] and hexagonal boron nitride [23]. The description of the measured $f_m(T)$ with the calculated $\alpha_{WSe_2}(T)$ is obtained using Eq. 5.2 with $V_g^{DC} \approx \Delta\phi$ and

$$\varepsilon = \varepsilon_0 + \int_{T=300K}^{T} \alpha(T_0)\mathrm{d}T, \tag{5.3}$$

using the built-in strain ε_0 at room temperature as a fitting parameter (Fig. 5.9b); the best agreement between the measurements and

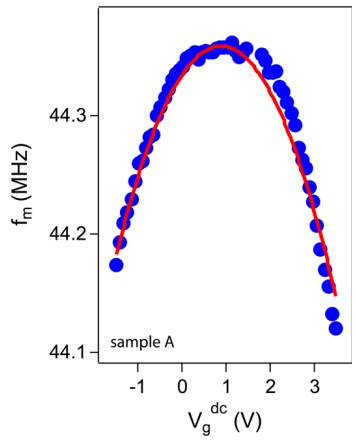

FIGURE 5.10: f_m as a function of the backgate voltage measured at 130 K. The red curve is the capacitive softening quantified by eq 5.2. We set V_g^{AC} = 10 mV.

Eq. 5.2 is obtained with ε_0 = 0.034%. The thermal expansion of the substrate contributes to ε by a small amount since $\alpha_{Si}(T)$,$\alpha_{SiO_2}(T) \ll \alpha_{WSe_2}(T)$; an upper bound of the substrate contribution to the resonant frequency is indicated by the gray area in Fig. 5.9b. The temperature dependence of the resonance frequency of the two measured WSe_2 resonators (Fig. 5.9a and Fig. 5.9b) are very similar similar, which further confirms the thermal expansion coefficient in Fig. 5.9c. Overall, our measurements show that the thermal expansion coefficient of WSe_2 is positive and reaches a high value at room temperature ($\alpha_{WSe_2}(T = 300K) \sim 7x10^6$ K^{-1}). The precise knowledge of the thermal coefficient of WSe_2 over a wide temperature range is important for heat management and designing future (opto-) electronic van der Waals heterostructures.

5.4.1 Discussion on the high Q-factor measured at helium temperature

High Q-factors are also observed in resonators based on other TMD monolayers, such as MoS_2 and $MoSe_2$. Fig. 5.11 shows the Q-factor of all the seven TMD resonators measured at helium temperature with $P < 10$ μW. The corresponding spectra are shown in Fig. 5.2. All the observed Q-factors are at least 1 order of magnitude higher than the values reported previously and measured at room temperature.

The origin of the high Q-factors achieved in this work can be attributed to a combination of different factors. First, the low amount of adsorbed molecules is beneficial, because such contamination can

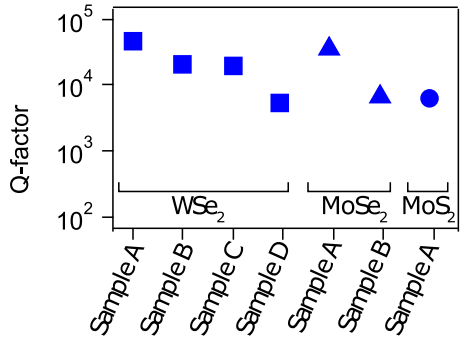

FIGURE 5.11: Quality factors of various resonators based on WSe_2, $MoSe_2$ and MoS_2 monolayers. The measurements are carried out at helium temperature with $P < 10\ \mu W$.

increase dissipation through two-level systems [74, 75] and the diffusion of adsorbed molecules [76]. Second, the phonon spectrum of TMDs is expected to result in higher Q-factors compared to graphene, because of the lower phonon−phonon scattering rate [77]. Third, the strain of the suspended monolayer can lead to the enhanced Q, since the Q-factor and the resonance frequency vary strongly in the same temperature range, that is, between ∼80 and 300 K. The quality factor $Q = f_m/\Gamma_m$ is indeed expected to get larger when f_m increases, assuming that Γ_m remains constant [78–80]. However, the increase of f_m by a factor 2 can only explain part of the factor ∼100 enhancement of the Q-factor. The strong temperature dependence of the Q-factor can be associated with the spectral broadening that arises from the interplay of the amplitude fluctuations of thermal vibrations and nonlinearities, such as the Duffing nonlinearity and mode−mode coupling [81–83]. Such spectral broadening is expected to reduce for larger strain, as is observed in our experiments. The effect of spectral broadening can be tested with ring-down experiments [66] but measuring the ring-down in our devices requires large laser power, such that the mechanical line width becomes limited by dynamical photothermal damping. Further work is needed to clarify the underlying physics governing our observed temperature dependence of the Q-factor.

5.5 Conclusions

We have reported an ultrasensitive optical readout of monolayer TMD resonators that allows us to reveal their mechanical properties at cryogenic temperatures. We report Q-factors up to $4.7\text{x}10^{-4}$ at 3.5 K, thus surpassing the Q-factor of graphene nanoresonators with similar areas. High Q-factors are obtained using low laser power in order to

prevent absorption heating and by tuning the back-gate voltage so that the damping contribution due to the electron-vibration coupling is negligible. Upon cooling the resonators, the resonant frequency increases steadily, which is due to the thermal contraction of the monolayer crystal. Because of the combination of the high mechanical Q-factor and its fascinating optical properties, TMD monolayer provides a unique platform for nano-optomechanics.

Chapter 6

Optomechanical measurement of the thermal transport proprieties of transition metal dichalcogenide monolayers

6.1 Introduction

This work is under submission [Nicolas morell, Slaven Tepsic, Antoine Reserbat-Plantey, Andrea Cepellotti, Marco Manca, Andreas Isacsson, Xavier Marie, Francesco Mauri, Adrian Bachtold].

Exquisite motion sensing is central to the celebrated results of modern gravitational wave detectors [84]. It also opens new possibilities in condensed-matter physics, with recent advances in fields related to nano-magnetism [85, 86], persistent currents in normal metal rings [87], and engineered electron-phonon coupling [88]. Here we show how optomechanical systems can be used to study heat transport in low-dimensional materials. Heat transport at the nanoscale is of major fundamental interest for a broad range of research fields, such as nanophononics [89], spintronics [90], and quantum thermodynamics [91].

Phonons are the main carriers of heat in a large variety of low-dimensional materials, including carbon nanotubes [28, 29], graphene [32], and semiconductor monolayers [40]. Heat transport enters into interesting regimes at low temperature, such as the dissipationless transport through low-dimensional materials in the ballistic regime [28, 30, 92]. However, measuring the thermal conductance at cryogenic temperature remains a challenging task. It requires the fabrication of

sophisticated devices, which incorporate local heaters and thermometers, and a careful calibration of the latter. A complication for interpreting these measurements comes from the fact that the thermal conductance depends on various quantities that have not been measured independently thus far. These include the heat capacity and the phononic mean-free path.

Heat transport measurements in low-dimensional materials have so far consisted in probing the thermal conductance K, that is, how well the system conducts heat. In optomechanics, it is possible to measure how quickly the mechanical resonator conducts heat [8, 9]. The characteristics time τ for the heat to travel out of the resonator introduces a retarded force acting on the mechanical resonator [5, 7]. We combine both methods to measure K and τ in a optomechanical resonator based on a vibrating $MoSe_2$ monolayer. This allows us to unravel the thermal properties of low-dimensional materials in an unprecedented way, down to cryogenics temperature, and with a device that is simple to fabricate.

6.2 Device characterization

The mechanical resonator consists of a $MoSe_2$ monolayer drum (Fig. 6.1a,b). The fabrication of the device and the measurment priciples are the same as those in Ch. 5. The device is fabricated by transferring a $MoSe_2$ monolayer over a substrate with a circular hole. The mechanical vibrations (Fig. 6.1a,d) are detected by optical interferometry [7].

We select $MoSe_2$ monolayers using optical microscopy measurements for the fabrication of devices Fig. 6.1. We use low-temperature photoluminescence measurements to confirm that fabricated devices consist of monolayer flakes (Fig. 6.2). The spectrum shows the exciton and the trion peaks of $MoSe_2$ monolayers.

We carry out optomechanical experiments on stretched membranes. As in the previous chapter, we estimate the strain from the measured dependence of the resonant frequency on the gate voltage shown in Fig. 6.3 using the expression

$$f_{\mathrm{m}}(V_{\mathrm{g}}^{\mathrm{DC}}) = \frac{1}{2\pi}\sqrt{\frac{4.92E_{2\mathrm{D}}}{m_{\mathrm{eff}}}\epsilon - \frac{\varepsilon_0}{d^3}\frac{0.271\pi R_0^2}{m_{\mathrm{eff}}}(V_{\mathrm{g}}^{\mathrm{DC}}+\Delta\phi)^2}, \qquad (6.1)$$

where $E_{2\mathrm{D}}$ corresponds to the two dimensional young modulus of $MoSe_2$, R_0=2.5 μm is the radius of the resonator, d=200 nm is the effective distance between the gate and the membrane (taking into account the dielectric constant of the substrate), and $\Delta\phi$ is the work function difference between the gate electrode and the resonator. We obtain the effective mass m_{eff} from the curvature of the parabola. We then estimate the strain from the resonant frequency at $V_{\mathrm{g}}^{\mathrm{DC}} = \Delta\phi$ (see Ch.

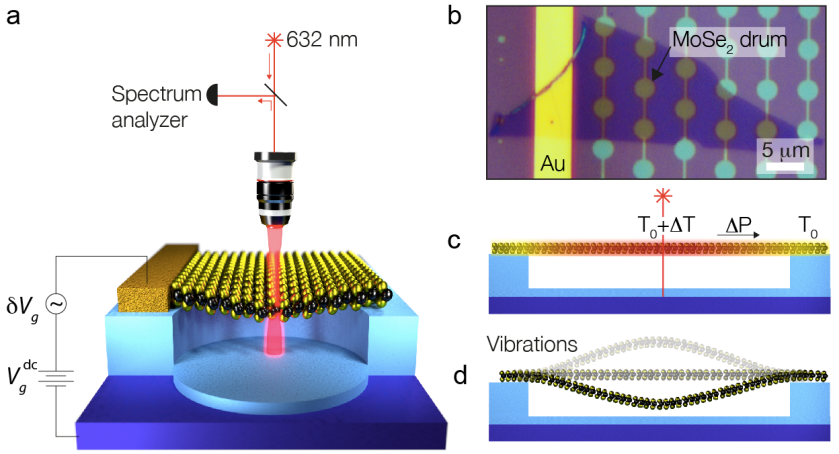

FIGURE 6.1: (a) Schematic of the optomechanical device. The transition metal dichalcogenide monolayer drum [43, 68] is fabricated with the dry transfer of thin $MoSe_2$ crystals over prestructured holes. The mechanical vibrations are driven capacitively and detected by optical interferometry [93]. The $MoSe_2$ monolayer is a mobile absorber in an optical standing wave produced by a 632 nm probe laser. The modulated laser reflection intensity is measured with an avalanche photo-detector feeding a spectrum analyzer. (b) Optical microscopy image of a typical device. (c) Heat transport induced by the absorption of the laser power. A temperature difference ΔT is created from the heat flow. (d) Detection of the laser-induced temperature rise ΔT using the fundamental mechanical mode of the optomechanical resonator.

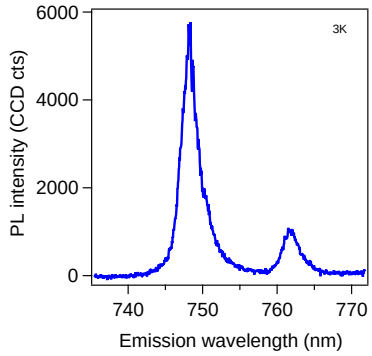

FIGURE 6.2: Photoluminescence spectrum of the $MoSe_2$ monolayer used to fabricate the 2.5 and 1.5 μm radius drums. The spectrum is recorded using a HeNe laser with 20 μW power. The background of the spectrum is substracted.

5). In all our $MoSe_2$ drums we obtain a positive strain in the range 0.1-1%. The fact that our drums are under tension is confirmed by the strong temperature dependence of the resonant frequency shown in Fig. 6.5a. The latter behavior is attributed to the thermal contraction of the $MoSe_2$ crystal when lowering temperature (Ch. 5). The positive strain at room temperature arises from the built-in stress created during fabrication (Ch. 5).

These measurements show that the membrane is flat when $\Delta V_g^{DC} = (V_g^{DC} - \Delta\phi) \simeq 0$, while it becomes bent at finite ΔV_g^{DC} due to the electrostatic force. We estimate that the central position of our drums is deflected by about $\leq$10 nm when $\Delta V_g^{DC} = 4V$. Fig. 6.3 shows that $\Delta\phi \simeq$0.2V for the 2.5 μm radius drum discussed in the main text.

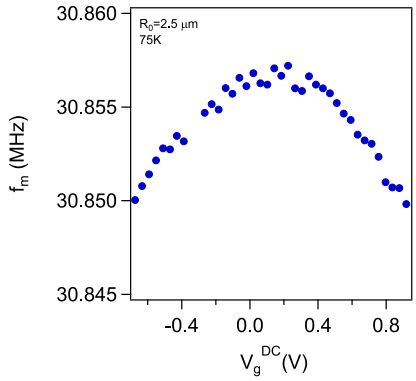

FIGURE 6.3: Mechanical resonance frequency as a function of static gate voltage.

The intensity of the laser oscillates as a function of the coordinate in the direction perpendicular to the substrate surface because of the interference between the incident and the reflected beam. Fig. 6.4 shows the calculated intensity profile I(z) normalized to the intensity I_0 of the incident beam for our device layout. The oscillation of I/I_0 is limited between 0.4 and 1.3 because of the absorption of the Si substrate. The intensity of the beam is $0.5 \cdot I_0$ at the level of the monolayer. The intensity profile in Fig. 6.4 is obtained using the Lumerical FDTD full wave simulation. We use 5.7 % for the absorption coefficient from the measurements in Ref. [41] . Overall, we have that the absorbed laser power is $P=0.5 \cdot 0.057 \cdot P_0$ where P_0 is the measured power of the incident laser.

We verify that the absorption of $MoSe_2$ monolayers at 633 nm remains constant when varying the temperature from 3 to 300 K and when sweeping the gate voltage from – 4 V to +4 V. We carry out the measurements on $MoSe_2$ monolayers transferred on Si chips. We study the absorption by comparing the measured reflection power

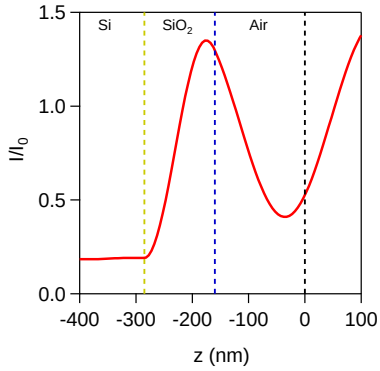

FIGURE 6.4: Simulated intensity profile of the normalised laser intensity in the direction perpendicular to the substrate. The black dashed line at z=0 nm corresponds to the position of the monolayer. The wavelength of the laser beam is 633 nm.

when the laser beam is focused on the $MoSe_2$ monolayer and when it is focused nearby the monolayer. This measurements were made in collaboration with Xavier Marie and Marco Manca (INSA, Toulouse, France).

6.3 Measurement technique

As explained in Ch. 2 the fact of measuring the mechanical resonator with the laser beam modifies the dynamics of the mechanical vibrations by a small amount. This backaction has two components, the static and the dynamical backaction. The former allows us to quantify K, and the latter τ

6.3.1 Optomechanical measurement of the equivalent thermal conductance

In Ch. 3 we introduced the Raman measurement used to quantify the thermal conductivity of 2D materials. We measure the thermal conductance in a way similar to this well-established method [35, 36].

The laser beam is focused onto the center of the $MoSe_2$ membrane. The static backaction is a simple absorption heating effect, which results in a temperature gradient ΔT between the center of the membrane and its circular clamp (Fig. 6.1c). The heat flow is given by the power ΔP absorbed in the membrane. In a Raman measurement, ΔT is quantified by the frequency shift of Raman-active peaks. In our case, ΔT is measured by the frequency shift Δf_T of the fundamental mechanical mode (Fig. 6.1d). We measure the shift of the resonant

frequency when the absorbed laser power P is increased in order to get $\Delta P = \frac{\delta f_m}{\delta P}$ (Fig. 6.5b,d). We assume that the absorbed energy is entirely transferred into the phonon modes of the crystal as in the Raman method. As a calibration, we measure the resonant frequency as a function of the temperature of the cryostat, that is, $\Delta T = \frac{\delta f_m}{\delta T}$ (Fig. 6.5a,c). As a result, the equivalent thermal conductance is

$$K = \frac{\Delta P}{\Delta T} = \frac{\delta f_m / \delta T}{\delta f_m / \delta P}. \tag{6.2}$$

Mechanical $MoSe_2$ drums with their high quality factor [93] are extremely good temperature sensors, allowing us to measure the linear thermal conductance down to 3 K. This is a significant improvement compared to Raman measurements, which are typically operated at 300K or above.

6.3.2 Measurement of the photothermal characteristic time

There is a static and a dynamical backaction of the laser beam on the dynamics of the resonator. The static backaction is a simple absorption heating effect that increases the temperature of the resonator as discussed above. It shifts the resonant frequency by Δf_T and the damping rate by $\Delta\Gamma_T$. The dynamical backaction is related to the retardation of the photothermal force τ. We measure τ from the effect of the dynamical backaction on the electrostically driven vibrations. Absorption heating from the laser beam expands the $MoSe_2$ crystal [93], which is equivalent to a force acting on the membrane. The crystal expansion responds to a change in the absorbed laser power with delay, that is, the time τ for the membrane to heat up or to cool down. The absorbed laser power oscillates in time because of the oscillating motion of the membrane in the laser interference pattern used to detect the vibrations. Overall, the photothermal force oscillates with a finite phase shift compared to the motion of the membrane. The in-phase photothermal force modifies the resonance frequency by Δf_B and the out-of-phase photothermal force modifies the mechanical linewidth by $\Delta\Gamma_B$ as seen in Ch. 2

$$\Delta(f_B)^2 = f_m^2 \frac{dF}{dz}\frac{1}{k}\frac{1}{1+(2\pi f_m)^2\tau^2}, \tag{6.3}$$

$$\Delta\Gamma_B = -\Delta\Gamma_m Q \frac{dF}{dz}\frac{1}{k}\frac{2\pi f_m \tau}{1+(2\pi f_m)^2\tau^2}, \tag{6.4}$$

here f_m is the resonance frequency of the mechanical mode, k the spring constant, z the coordinate in the direction perpendicular to the

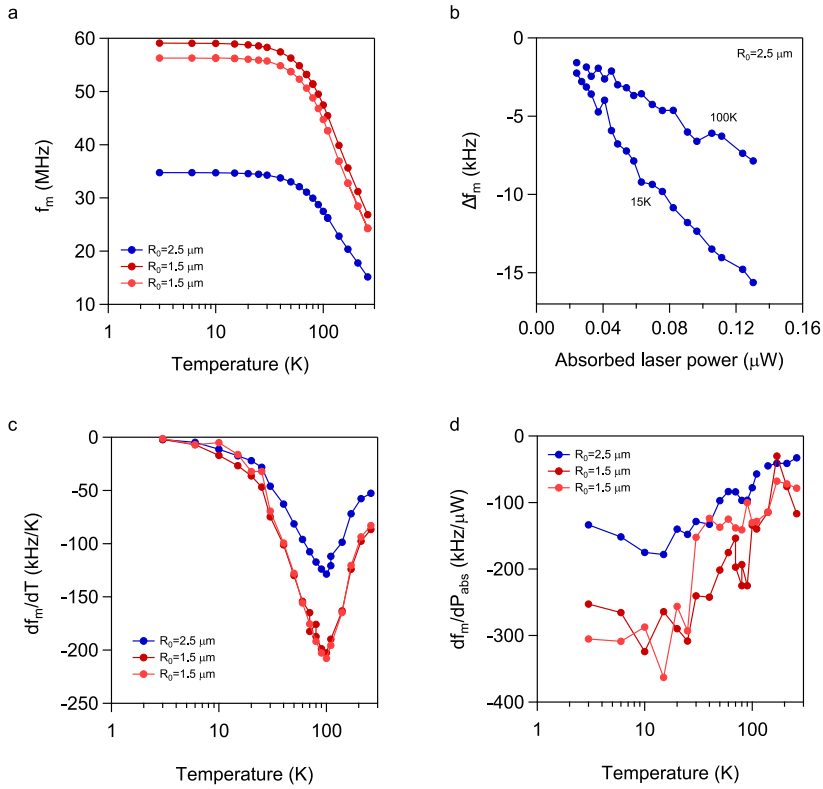

FIGURE 6.5: a) Resonance frequency of the mechanical mode as a function of temperature for three different devices. (b) Shift of the resonance frequency Δf_{m} as a function of absorbed laser power ΔP when the drum is in the straight configuration. The temperature difference ΔT is obtained from Δf_{m} using the calibration slope $\Delta f_{\mathrm{m}}/\Delta T$ in (a). The conductance is measured in the linear regime, because the applied ΔP is low. The largest ΔT remains below 1 K. (c) and (d) are the numerical derivatives of (a) and (b) respectively.

membrane, and $\frac{dF}{dz}$ the derivative of the z-component of the photothermal force with respect to z. We have $\frac{dF}{dz} \propto P$ and $Q = \frac{f_{\mathrm{m}}}{\Delta\Gamma_{\mathrm{m}}}$. We infer τ from Δf_{B} and $\Delta\Gamma_{\mathrm{B}}$ for a fixed laser power using

$$\tau = \frac{\Delta\Gamma_{\mathrm{B}}}{4\pi^2\Delta(f_{\mathrm{B}})^2} = \frac{\Delta\Gamma_{\mathrm{B}}}{4\pi f_{\mathrm{m}}\Delta f_{\mathrm{B}}}. \tag{6.5}$$

Dynamical backaction in our device layout can be controlled with the voltage applied to the backgate of the wafer. The backaction force vanishes to zero for zero gate voltage when the membrane is flat, because the photothermal force is perpendicular to the displacement (Fig. 6.6).

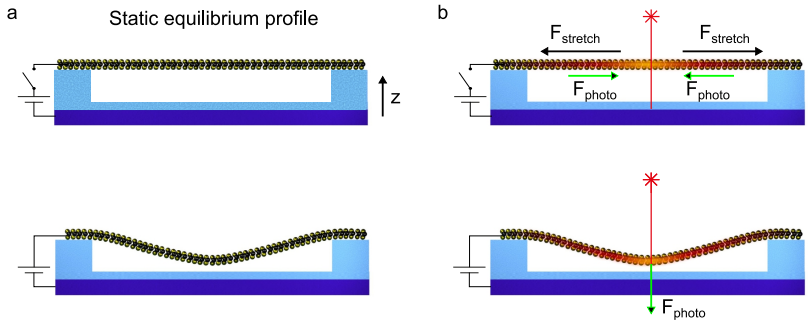

FIGURE 6.6: Cross section of the suspended monolayer membrane coupled to the laser beam. (a) At $\Delta V_g^{DC} \simeq 0$ the membrane is flat, while a finite gate voltage deflects the membrane. (b) When the membrane is flat, the dynamical backaction is suppressed to zero. Indeed, the thermal expansion of the crystal results in a force that cannot drive flexural vibrations. The force is perpendicular to the displacement. When the membrane is bent with a finite gate voltage, the dynamical backaction becomes finite, because the photothermal force can drive the resonator.

Since the static and the dynamical backactions vanish to zero at zero laser power, we linearize the measured frequency f_m and damping rate $\Delta\Gamma_m$as functions of absorbed laser power P_{abs} (Fig. 6.7).

$$f_m(P) = f_m(P=0) + aP_{abs}, \tag{6.6}$$

$$\Gamma_m(P) = \Gamma_m(P=0) + bP_{abs}. \tag{6.7}$$

At $\Delta V_g^{DC} \simeq 0V$ there is static backaction, but no dynamical backaction (Fig. 6.6),

$$\Delta f_T(P) = a_{0V} P_{abs}, \tag{6.8}$$

$$\Delta\Gamma_T(P) = b_{0V} P_{abs}. \tag{6.9}$$

At $\Delta V_g^{DC} = 4V$there are both static and dynamical backactions (Fig. 6.6),

$$\Delta f_T(P) + \Delta f_B(P) = a_{4V} P_{abs}, \tag{6.10}$$

$$\Delta\Gamma_T(P) + \Delta\Gamma_B(P) = b_{4V} P_{abs}. \tag{6.11}$$

The static dynamical backaction is expected to weakly change when varying the gate voltage by a few volts, because the static displacement remains small. Therefore,

$$\Delta f_B(P) = a_{0V} P_{abs} - a_{4V} P_{abs}, \tag{6.12}$$

$$\Delta\Gamma_B(P) = b_{0V}P_{abs} - b_{4V}P_{abs}. \tag{6.13}$$

As a result Eq. 6.5 becomes,

$$\tau = -\frac{b_{0V} - b_{4V}}{4\pi f_0(a_{0V} - a_{4V})}. \tag{6.14}$$

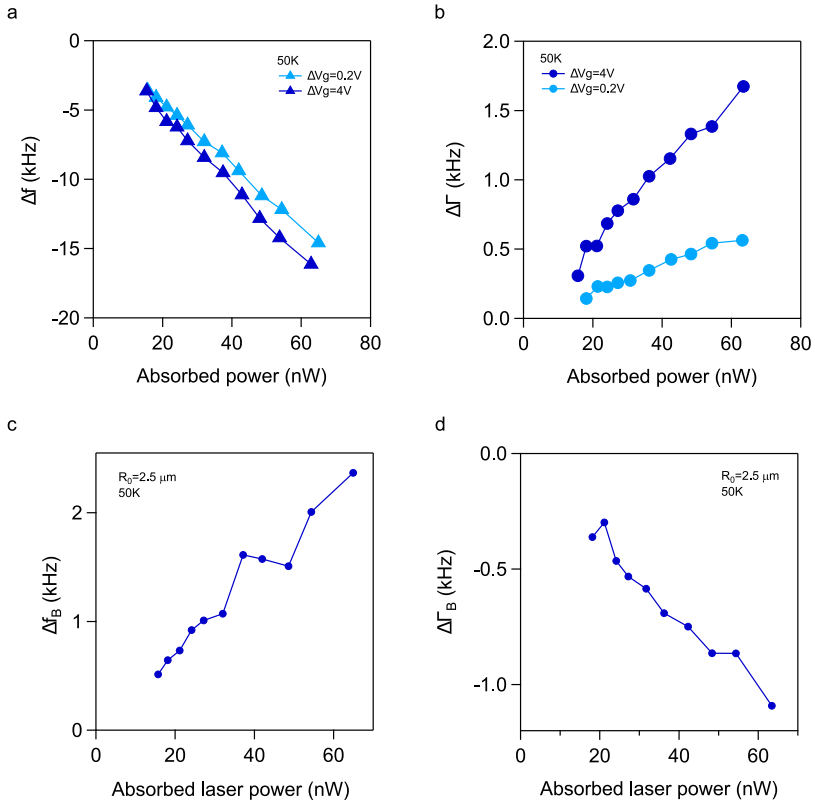

FIGURE 6.7: Measured variations of the resonant frequency (a) and damping (b) as functions of laser power for two different gate voltages. The dynamical backaction force is finite at $\Delta V_g^{DC} = 4V$, while is suppressed to zero at , while is suppressed to zero at $\Delta V_g^{DC} \simeq 0V$,see Fig. 6.6. (**c,d**) Shifts of the resonance frequency Δf_B and the mechanical bandwidth $\Delta\Gamma_B$ as a function of absorbed laser power ΔP. We obtain Δf_B and $\Delta\Gamma_B$ by subtracting the frequency shift and the bandwidth shift measured in the bending configuration from that measured in the straight configuration (a) and (b) respectively

6.4 Equivalent thermal conductance and characteristic photothermal time

The temperature dependance of the thermal conductance suggests the crossover between ballistic and diffusive regimes (Fig. 6.8a). Below $\sim$ 100 K, the conductance gets larger when increasing temperature, which indicates ballistic transport. In this regime, the mean-free path is expected to be given by the characteristic size of the drum. Upon increasing temperature above $\sim$ 100 K, the conductance starts to decrease, which is attributed to the reduction of the mean-free path due to phonon-phonon scattering.

Ballistic transport below 100 K is further supported by dynamical backaction measurements. Figs. 6.7c,d and 6.8b show that τ remains constant in this temperature range within the error bars of the measurements. We cannot measure τ above $\sim$100 K, since the reduced quality-factor prevents us to resolve Δf_B. The average time $\langle\tau\rangle = 3.3$ ns associated to the averaged phonon velocity $v \simeq 1300$ m/s computed by first principles gives a characteristic length of about 4.3 μm, which is consistent with the 2.5 μm radius of the drum.

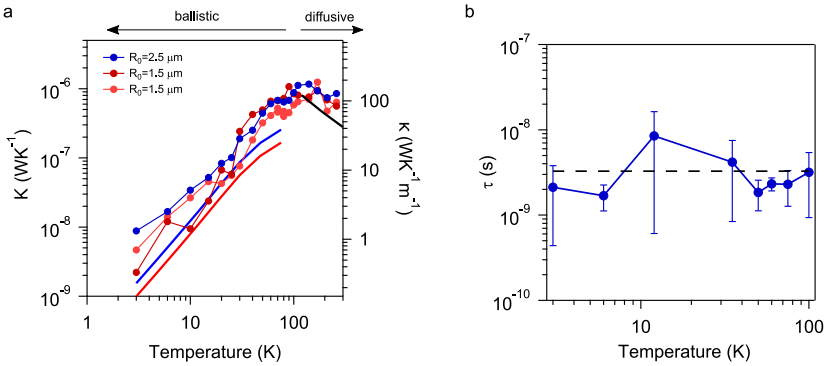

FIGURE 6.8: (a) Thermal conductance $K = \Delta P/\Delta T$ as a function of temperature. The right axis shows the conductivity in the diffusive regime, which is obtained using Eq. 6.19 with η=0.61. The black line shows the conductivity computed in the diffusive regime for an infinitely large monolayer. The red and the blue line corresponds to the conductance in the ballistic regime computed from first principles for the 1.5 and the 2.5 μm radius drum, respectively, using Eq. 6.20 with $\alpha = 2.1$ and $\alpha = 3.2$. (b) Time for the heat to travel out of the drum as a function of temperature. The large error bars at 12 and 35 K are due to the drift of the resonance frequency caused by the automatized heating and cooling switches in our cryofree cryostat. The dashed black line corresponds to the averaged τ.

6.5 Equivalent heat capacity

The thermal conductivity and the τ measurements allow us to directly quantify the equivalent heat capacity of an individual $MoSe_2$ monolayer. The thermal transport in our experiment can be seen as the unidirectional flow of energy from the laser beam into the monolayer membrane in a first step, and from the membrane to the environment in a second step (Fig. 6.9a). We assume that all energy absorbed into the membrane flows to the environment via the phononic states of the crystal – this is the assumption made in the Raman measurements of thermal transport [35–42]. Because of the conservation of the heat flow, the power P_{in} flowing into the monolayer crystal is equal to the power P_{out} flowing out of the crystal. Here, P_{in} is the absorbed power P of the laser, and P_{out} is related to the heat-induced energy shift $\Delta E_{\text{monolayer}}$ (stored in the monolayer crystal) multiplied by the energy escape rate $1/\tau$. This rate is given by the inverse of the measured characteristic time τ for the crystal to heat or to cool down. We have

$$P_{\text{in}} = P, \tag{6.15}$$

$$P_{\text{out}} = \frac{\Delta E_{\text{monolayer}}}{\tau}. \tag{6.16}$$

Setting $P_{\text{in}} = P_{\text{out}}$, we define the equivalent heat capacity

$$C = \frac{\Delta E_{\text{monolayer}}}{\Delta T} = \tau \cdot K. \tag{6.17}$$

Fig. 6.9b shows that the temperature dependence of the heat capacity approaches a T^2 dependence. This is consistent with the T^d dependence expected for two-dimensional systems in its simplest form, where $d = 2$ is the dimensionality. Previous measurements of the phononic heat capacity of nano-materials were carried out by packing them in macroscopic ensembles, such as films of nanotube ropes [94] and powders of $MoSe_2$ multilayered crystals [95]. Such ensemble measurements suffer from the coupling between nano-systems, which modifies the heat capacity at low temperature.

6.6 Thermal conductivity and specific heat capacity

The temperature profile along the heat flow has to be considered when evaluating the specific heat capacity and the thermal conductivity of $MoSe_2$ monolayers (Figs. 6.8a and 6.9b). In the ballistic regime, the temperature drops as $1/r$ along the radial coordinate r because of the conservation of heat flow in our disc geometry. This contrasts with the

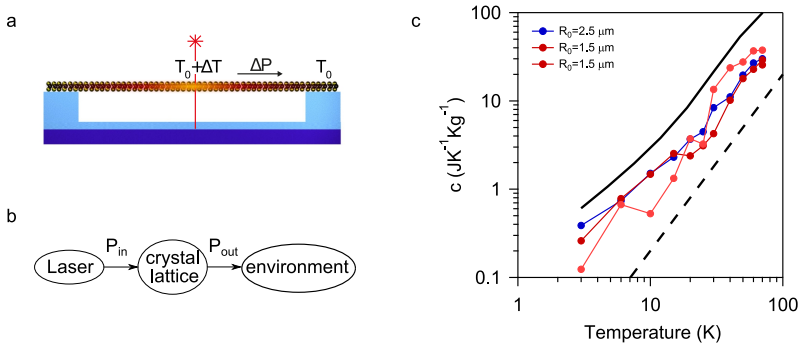

FIGURE 6.9: (a) Monolayer membrane coupled to a focused laser beam. The laser acts as a local heat source. The heat travels through the monolayer crystal from the center of the crystal to its circular clamping edge. Because of the thermal resistance, the heat flow ΔP leads to a temperature gradient ΔT. The yellow region corresponds to higher temperature, while red black regions correspond to lower temperature. (b) Schematic of the power flow. The power P_{in} flowing into the monolayer crystal is equal to the power P_{out} flowing out the crystal. (**c**) Specific heat capacity as a function of temperature. We convert $C = \langle\tau\rangle K$ into c using Eq. 6.18 with $\beta = 0.86$. The black dashed line corresponds to the T^2 dependence. The black continuous line corresponds to the specific heat capacity computed from first-principles. Since the displacement sensitivity of the 1.5 μm radius drums was not good enough to measure τ, we estimate $\langle\tau\rangle$ from the value measured with the 2.5 μm radius drum and the radius ratio.

constant temperature profile along ballistic conductors with uniform width. In the diffusive regime, the temperature decreases logarithmically along r due to phonon scattering events. The measured C and K are converted into the specific heat capacity c and the thermal conductivity κ using

$$c = \frac{C}{\pi R_0^2 t \rho}\beta, \tag{6.18}$$

$$\kappa = \frac{K}{2\pi t}\eta, \tag{6.19}$$

where R_0 is the radius of the suspended drum, $t = 0.64$ nm the thickness of the monolayer, and ρ the mass density of $MoSe_2$. The constants β and η are of the order of one and depend on R_0, the radius r_0 of the laser beam, and the temperature profile. The conductivity is meaningful in the diffusive regime only (Fig. 6.8a).

The measured temperature dependencies of c, K in the ballistic regime, and κ in the diffusive regime are well described by first-principles calculations on $MoSe_2$ monolayers (Figs. 6.8a and 6.9b). For this, we derive the ballistic conductance in our peculiar disc geometry assuming that the inner reservoir is given by the radius r_0, and the outer reservoir by R_0. We obtain

$$K = 2\pi r_0 t \alpha \cdot \frac{\rho c v}{2}, \tag{6.20}$$

$$v = \frac{\sum_{q,s} C_{q,s} \frac{2|v_{q,s}|}{\pi}}{\sum_{q,s} C_{q,s}}, \tag{6.21}$$

where $C_{q,s} = \frac{dn_{q,s}}{dT}\hbar\omega_{q,s}$ is the specific heat of the phonon of the branch s with momenta q, $\omega_{q,s}$ the phonon pulsation, $n_{q,s}$ the Bose occupation factor, and $v_{q,s}$ the group velocity. The constant α is also of the order of one. The phonon properties of the monolayer lattice are calculated using density functional perturbation theory. The conductivity is derived using the Boltzmann transport equation taking into account three-phonon interactions and isotopic scattering in the diffusive regime [96]. The derivation of Eqs. 6.18-6.20 and the first-principle calculations were performed by Andrea Cepellotti (University of California at Berkeley, California, USA), Andreas Isacsson (Chalmers University, Goteborg, Swedden) and Francesco Mauri (La Sapienza, Rome, Italy).

6.7 Conclusions

Our optomechanical measurements provide a clear and detailed picture of thermal transport in monolayer $MoSe_2$ lattices down to cryogenic temperature. Our work opens the possibility to measure thermal properties in a large variety of different two-dimensional materials, because the devices required for these measurements are simple to fabricate. This new measurement method may allow the exploration of the phonon hydrodynamics regime, which is expected to be robust in monolayer systems [34, 97]. This regime is interesting because heat is carried by collective excitations of phonon states. This gives rise to a new type of sound propagation, called second sound. The measurement of τ should enable the direct access of the velocity of the second sound. In addition, this new measurement method may shed light on the divergence of the thermal conductivity in two-dimensions, when the size of the system increases [30]. The origin of this behaviour is under active investigation with different interpretations based on either the dimensionality of the system or the special phononic states that remain ballistic over extraordinarily long distances [33, 98, 99]. Moreover, the measurement of the specific heat holds promise for studying phase transitions of electronic many-body collective phenomena in monolayers, including the charge density wave order and unconventional superconductivity [100, 101].

Chapter 7

Conclusions and Outlook

In the Chapter 4 of this thesis it has been shown that relaying on a robust and rather simple fabrication technique, it is possible to produce ultra high Q-factor resonators based on single layer TMD. The Q-factors have been studied in Chapter 5 in order to understand the origin of its low dissipation. We propose that the suppression of phono-phonon interactions is an important ingredient for the dramatic increase of the Q-factors when temperature is lowered. The study of the temperature dependence of the resonance frequency allowed us to prove the positive thermal expansion coefficient of TMDs.

The high Q-factors opened the possibility of measuring mechanical vibrations of TMD resonators at unprecedented low laser power. This could be used in Chapter 6 to study thermal transport at cryogenic temperatures. The temperature dependence of quantities such as the thermal conductivity and the phonon mean free path were never measured before on a 2D material. These measurements reveal a transition from diffusive to ballistic thermal transport regime for these particular devices.

The extraction of thermal transport quantities such as the conductivity and the specific heat in 2D materials open the possibility for studying different materials that may show different transport regimes. By increasing the size of the resonators it is expected, specially in graphene, that it could be possible to observe the hydrodynamic thermal transport regime. It could also be possible to measure materials with other properties such as 2D superconductors like $NbSe_2$ and try to probe its superconductor phase transition.

Given the high Q-factors and the low mass of the resonators we envision hybrid optomechanics experiments in which mechanical vibrations are coupled to single quantum emitters embedded in the crystal via the strain field and to two-dimensional excitons and their valley pseudo-spins via a gradient of magnetic field. The mechanical vibrations of TMD monolayers can also be coupled to quantum emitters via the Casimir interaction. When placing a quantum emitter, such as a dibenzoterrylene (DBT) molecule, a few tens of nanometers away from the monolayer, vacuum fluctuations lead to extremely large dispersive couplings, opening new possibilities for quantum opto-mechanics

experiments.

Bibliography

[1] Ioannis Tsioutsios. "Mechanical Resonators Based on Graphene and Carbon Nanotubes". In: *PhD Thesis* (June 2016).

[2] Changyao Chen and James Hone. "Graphene nanoelectromechanical systems". In: *Proceedings of the IEEE* 101.7 (2013), pp. 1766–1779. ISSN: 00189219. DOI: 10.1109/JPROC.2013.2253291. arXiv: 1206.4363.

[3] P. Weber et al. "Coupling graphene mechanical resonators to superconducting microwave cavities". In: *Nano Letters* 14.5 (2014), pp. 2854–2860. ISSN: 15306992. DOI: 10.1021/nl500879k. arXiv: 1403.4792.

[4] Benjamin Lassagne et al. "Coupling mechanics to charge transport in carbon nanotube mechanical resonators". In: *Science* 325.5944 (2009), pp. 1107–1110.

[5] Constanze Höhberger Metzger and Khaled Karral. "Cavity cooling of a microlever". In: *Nature* 432.7020 (2004), pp. 1002–1005. ISSN: 00280836. DOI: 10.1038/nature03118.

[6] Juan Restrepo et al. "Classical and quantum theory of photothermal cavity cooling of a mechanical oscillator". In: *Comptes Rendus Physique* 12.9-10 (2011), pp. 860–870. ISSN: 16310705. DOI: 10.1016/j.crhy.2011.02.005. arXiv: 1011.3911. URL: http://dx.doi.org/10.1016/j.crhy.2011.02.005.

[7] Robert A. Barton et al. "Photothermal self-oscillation and laser cooling of graphene optomechanical systems". In: *Nano Letters* 12.9 (2012), pp. 4681–4686. ISSN: 15306984. DOI: 10.1021/nl302036x.

[8] Constanze Metzger et al. "Optical self cooling of a deformable Fabry-Perot cavity in the classical limit". In: *Physical Review B - Condensed Matter and Materials Physics* 78.3 (2008), pp. 1–12. ISSN: 10980121. DOI: 10.1103/PhysRevB.78.035309.

[9] Olivier Arcizet. "Ultrasensitive optical readout and radiation pressure cooling of a micro-mechanical resonator". In: *PhD Thesis* (2006).

[10] Hualing Zeng and Xiaodong Cui. "An optical spectroscopic study on two-dimensional group-VI transition metal dichalcogenides". In: *Chemical Society Reviews* 44.9 (2015), pp. 2629–2642. ISSN: 14604744. DOI: 10.1039/c4cs00265b. URL: http://dx.doi.org/10.1039/C4CS00265B.

[11] Ashwin Ramasubramaniam. "Large excitonic effects in monolayers of molybdenum and tungsten dichalcogenides". In: *Physical Review B - Condensed Matter and Materials Physics* 86.11 (2012), pp. 1–6. ISSN: 10980121. DOI: 10.1103/PhysRevB.86.115409. arXiv: 1403.3771.

[12] Mingu Kang et al. "Universal Mechanism of Band-Gap Engineering in Transition-Metal Dichalcogenides". In: *Nano Letters* 17.3 (2017), pp. 1610–1615. ISSN: 15306992. DOI: 10.1021/acs.nanolett.6b04775. arXiv: 1711.11236.

[13] Alexey Chernikov et al. "Electrical Tuning of Exciton Binding Energies in Monolayer WS2". In: *Physical Review Letters* 115.12 (2015), pp. 1–6. ISSN: 10797114. DOI: 10.1103/PhysRevLett.115.126802.

[14] Gang Wang et al. "Excitons in atomically thin transition metal dichalcogenides". In: Ml (2017). ISSN: 1539-0756. DOI: 10.1103/RevModPhys.90.021001. arXiv: 1707.05863. URL: http://arxiv.org/abs/1707.05863{\%}0Ahttp://dx.doi.org/10.1103/RevModPhys.90.021001.

[15] Keliang He et al. "Tightly Bound Excitons in Monolayer WSe_2". In: *Phys. Rev. Lett.* 113 (2 2014), p. 026803. DOI: 10.1103/PhysRevLett.113.026803. URL: https://link.aps.org/doi/10.1103/PhysRevLett.113.026803.

[16] Kin Fai Mak et al. "Atomically Thin MoS_2: A New Direct-Gap Semiconductor". In: *Phys. Rev. Lett.* 105 (13 2010), p. 136805. DOI: 10.1103/PhysRevLett.105.136805. URL: https://link.aps.org/doi/10.1103/PhysRevLett.105.136805.

[17] Malte Selig et al. "Excitonic linewidth and coherence lifetime in monolayer transition metal dichalcogenides". In: *Nature Communications* 7.May (2016). ISSN: 20411723. DOI: 10.1038/ncomms13279. arXiv: 1605.03359.

[18] G. Wang et al. "Valley dynamics probed through charged and neutral exciton emission in monolayer WSe2". In: *Physical Review B - Condensed Matter and Materials Physics* 90.7 (2014), pp. 1–6. ISSN: 1550235X. DOI: 10.1103/PhysRevB.90.075413. arXiv: 1402.6009.

[19] Deniz Çakır, François M. Peeters, and Cem Sevik. "Mechanical and thermal properties of h -MX ₂ (M=Cr, Mo, W; X=O, S, Se, Te) monolayers: A comparative study". In: *Applied Physics Letters* 104.20 (2014), p. 203110. ISSN: 0003-6951. DOI: 10.1063/1.4879543. URL: http://aip.scitation.org/doi/10.1063/1.4879543.

[20] Simone Bertolazzi, Jacopo Brivio, and Andras Kis. "Stretching and breaking of ultrathin MoS 2". In: *ACS Nano* 5.12 (2011), pp. 9703–9709. ISSN: 19360851. DOI: 10.1021/nn203879f.

[21] Ryan C. Cooper et al. "Nonlinear elastic behavior of two-dimensional molybdenum disulfide". In: *Physical Review B* 87.3 (2013), p. 035423. ISSN: 1098-0121. DOI: 10.1103/PhysRevB.87.035423. URL: https://link.aps.org/doi/10.1103/PhysRevB.87.035423.

[22] Duhee Yoon, Young Woo Son, and Hyeonsik Cheong. "Negative thermal expansion coefficient of graphene measured by raman spectroscopy". In: *Nano Letters* 11.8 (2011), pp. 3227–3231. ISSN: 15306984. DOI: 10.1021/nl201488g.

[23] C. Sevik. "Assessment on lattice thermal properties of two-dimensional honeycomb structures: Graphene, h -BN, h -MoS 2, and h -MoSe 2". In: *Physical Review B - Condensed Matter and Materials Physics* 89.3 (2014), pp. 1–5. ISSN: 10980121. DOI: 10.1103/PhysRevB.89.035422.

[24] K Schwab et al. "Measurement of the quantum of thermal conductance". In: 1275.1997 (2000), pp. 1997–2000.

[25] W Fon et al. "Phonon scattering mechanisms in suspended nanostructures from 4 to 40 K". In: (2002), pp. 3–7. DOI: 10.1103/PhysRevB.66.045302.

[26] J S Heron et al. "Mesoscopic Size Effects on the Thermal Conductance of Silicon Nanowire 2009". In: (2009).

[27] I J Maasilta. "Two-dimensional phononic thermal conductance in thin membranes in the Casimir limit Two-dimensional phononic thermal conductance in thin membranes in the Casimir limit". In: 041704.2011 (2016). DOI: 10.1063/1.3675925. URL: https://doi.org/10.1063/1.3675925.

[28] P. Kim et al. "Thermal transport measurements of individual multiwalled nanotubes". In: *Physical Review Letters* 87.21 (2001), pp. 215502–1–215502–4. ISSN: 10797114. DOI: 10.1103/PhysRevLett.87.215502. arXiv: 0106578 [cond-mat].

[29] Choongho Yu et al. "Thermal conductance and thermopower of an individual single-wall carbon nanotube". In: *Nano Letters* 5.9 (2005), pp. 1842–1846. ISSN: 15306984. DOI: 10.1021/nl051044e. arXiv: 0512624 [cond-mat].

[30] Xiaodong Xu et al. “Spin and pseudospins in layered transition metal dichalcogenides”. In: *Nature Physics* 10.5 (2014), pp. 343–350. ISSN: 17452481. DOI: 10.1038/nphys2942. arXiv: arXiv:1605.01972.

[31] Dmitri K Efetov et al. “Fast thermal relaxation in cavity-coupled graphene bolometers with a Johnson noise read-out”. In: *Nature nanotechnology* (2018), p. 1.

[32] Alexander A. Balandin. “Thermal properties of graphene and nanostructured carbon materials”. In: *Nature Materials* 10.8 (2011), pp. 569–581. ISSN: 14764660. DOI: 10.1038/nmat3064. arXiv: 1106.3789. URL: http://dx.doi.org/10.1038/nmat3064.

[33] Giorgia Fugallo et al. “Thermal Conductivity of Graphene and Graphite: Collective Excitations and Mean Free Paths”. In: (2014).

[34] Andrea Cepellotti et al. “Phonon hydrodynamics in two-dimensional materials”. In: *Nature Communications* 6 (2015), pp. 1–7. ISSN: 20411723. DOI: 10.1038/ncomms7400. URL: http://dx.doi.org/10.1038/ncomms7400.

[35] Alexander A. Balandin et al. “Superior thermal conductivity of single-layer graphene”. In: *Nano Letters* 8.3 (2008), pp. 902–907. ISSN: 15306984. DOI: 10.1021/nl0731872. arXiv: 0802.1367v1.

[36] Weiwei Cai et al. “Thermal transport in suspended and supported monolayer graphene grown by chemical vapor deposition”. In: *Nano Letters* 10.5 (2010), pp. 1645–1651. ISSN: 15306984. DOI: 10.1021/nl9041966.

[37] Clement Faugeras et al. “Thermal Conductivity of Graphene in Corbino Membrane Geometry”. In: *ACS Nano* 4.4 (2010), pp. 1889–1892. ISSN: 1936-0851. DOI: 10.1021/nn9016229. URL: http://dx.doi.org/10.1021/nn9016229.

[38] Suchismita Ghosh et al. “Dimensional crossover of thermal transport in few-layer graphene”. In: *Nature Materials* 9.7 (2010), pp. 555–558. ISSN: 14764660. DOI: 10.1038/nmat2753. arXiv: 1003.5247. URL: http://dx.doi.org/10.1038/nmat2753.

[39] Jae Ung Lee et al. “Thermal conductivity of suspended pristine graphene measured by Raman spectroscopy”. In: *Physical Review B - Condensed Matter and Materials Physics* 83.8 (2011), pp. 1–4. ISSN: 10980121. DOI: 10.1103/PhysRevB.83.081419. arXiv: 1103.3337.

[40] Rusen Yan et al. “Thermal conductivity of monolayer molybdenum disulfide obtained from temperature-dependent Raman spectroscopy”. In: *ACS Nano* 8.1 (2014), pp. 986–993. ISSN: 19360851. DOI: 10.1021/nn405826k.

[41] Xian Zhang et al. "Measurement of Lateral and Interfacial Thermal Conductivity of Single- and Bilayer MoS2and MoSe2Using Refined Optothermal Raman Technique". In: *ACS Applied Materials and Interfaces* 7.46 (2015), pp. 25923–25929. ISSN: 19448252. DOI: 10.1021/acsami.5b08580. arXiv: 1509.07100.

[42] Marianna Sledzinska et al. "Record Low Thermal Conductivity of Polycrystalline MoS ₂ Films: Tuning the Thermal Conductivity by Grain Orientation". In: *ACS Applied Materials & Interfaces* (2017), acsami.7b08811. ISSN: 1944-8244. DOI: 10.1021/acsami.7b08811. URL: http://pubs.acs.org/doi/abs/10.1021/acsami.7b08811.

[43] Jaesung Lee et al. "High frequency MoS2 nanomechanical resonators". In: *ACS Nano* 7.7 (2013), pp. 6086–6091. ISSN: 19360851. DOI: 10.1021/nn4018872.

[44] Zenghui Wang et al. "Black phosphorus nanoelectromechanical resonators vibrating at very high frequencies". In: *Nanoscale* 7.3 (2015), pp. 877–884.

[45] Andres Castellanos-Gomez et al. "Deterministic transfer of two-dimensional materials by all-dry viscoelastic stamping". In: *2D Materials* 1.1 (2014), p. 011002. URL: http://stacks.iop.org/2053-1583/1/i=1/a=011002.

[46] Rui Yang et al. "Multilayer MoS2 transistors enabled by a facile dry-transfer technique and thermal annealing". In: *Journal of Vacuum Science & Technology B, Nanotechnology and Microelectronics: Materials, Processing, Measurement, and Phenomena* 32.6 (2014), p. 061203.

[47] Ajit Srivastava et al. "Valley Zeeman effect in elementary optical excitations of monolayer WSe2". In: *Nature Physics* 11.2 (2015), pp. 141–147. ISSN: 17452481. DOI: 10.1038/nphys3203. arXiv: 1407.2624.

[48] Ajit Srivastava et al. "Optically active quantum dots in monolayer WSe2". In: *Nature Nanotechnology* 10.6 (2015), pp. 491–496. ISSN: 17483395. DOI: 10.1038/nnano.2015.60. arXiv: 1411.0025. URL: http://dx.doi.org/10.1038/nnano.2015.60.

[49] Andrea Splendiani et al. "Emerging photoluminescence in monolayer MoS2". In: *Nano Letters* 10.4 (2010), pp. 1271–1275. ISSN: 15306984. DOI: 10.1021/nl903868w. arXiv: 1308.1834[cond-mat.mtrl-sci].

[50] G. Sallen et al. "Robust optical emission polarization in MoS 2 monolayers through selective valley excitation". In: *Physical Review B - Condensed Matter and Materials Physics* 86.8 (2012), pp. 3–6. ISSN: 10980121. DOI: 10.1103/PhysRevB.86.081301. arXiv: 1206.5128.

[51] D. Lagarde et al. “Carrier and polarization dynamics in monolayer MoS 2”. In: *Physical Review Letters* 112.4 (2014), pp. 1–5. ISSN: 00319007. DOI: 10.1103/PhysRevLett.112.047401. arXiv: 1308.0696.

[52] M. Koperski et al. “Single photon emitters in exfoliated WSe2structures”. In: *Nature Nanotechnology* 10.6 (2015), pp. 503–506. ISSN: 17483395. DOI: 10.1038/nnano.2015.67. arXiv: 1411.2774. URL: http://dx.doi.org/10.1038/nnano.2015.67.

[53] Aaron M. Jones et al. “Optical generation of excitonic valley coherence in monolayer WSe 2”. In: *Nature Nanotechnology* 8.9 (2013), pp. 634–638. ISSN: 17483395. DOI: 10.1038/nnano.2013.151. arXiv: 1303.5318.

[54] G. Aivazian et al. “Magnetic control of valley pseudospin in monolayer WSe2”. In: *Nature Physics* 11.2 (2015), pp. 148–152. ISSN: 17452481. DOI: 10.1038/nphys3201. arXiv: 1407.2645.

[55] Chitraleema Chakraborty et al. “Voltage-controlled quantum light from an atomically thin semiconductor”. In: *Nature Nanotechnology* 10.6 (2015), pp. 507–511. ISSN: 17483395. DOI: 10.1038/nnano.2015.79. arXiv: 1109.3412. URL: http://dx.doi.org/10.1038/nnano.2015.79.

[56] Yu Ming He et al. “Single quantum emitters in monolayer semiconductors”. In: *Nature Nanotechnology* 10.6 (2015), pp. 497–502. ISSN: 17483395. DOI: 10.1038/nnano.2015.75. arXiv: 1411.2449. URL: http://dx.doi.org/10.1038/nnano.2015.75.

[57] J Scott Bunch et al. “Electromechanical resonators from graphene sheets”. In: *Science* 315.5811 (2007), pp. 490–493.

[58] Vibhor Singh et al. “Probing thermal expansion of graphene and modal dispersion at low-temperature using graphene nanoelectromechanical systems resonators”. In: *Nanotechnology* 21.16 (2010). ISSN: 09574484. DOI: 10.1088/0957-4484/21/16/165204. arXiv: 1001.4377.

[59] Tengfei Miao et al. “Graphene nanoelectromechanical systems as stochastic-frequency oscillators”. In: *Nano Letters* 14.6 (2014), pp. 2982–2987. ISSN: 15306992. DOI: 10.1021/nl403936a.

[60] A. Eichler et al. “Nonlinear damping in mechanical resonators made from carbon nanotubes and graphene”. In: *Nature Nanotechnology* 6.6 (2011), pp. 339–342. ISSN: 17483395. DOI: 10.1038/nnano.2011.71. arXiv: 1103.1788. URL: http://dx.doi.org/10.1038/nnano.2011.71.

[61] Changyao Chen et al. “Performance of monolayer graphene nanomechanical resonators with electrical readout”. In: *Nature Nanotechnology* 4.12 (2009), pp. 861–867. ISSN: 17483395. DOI: 10.1038/nnano.2009.267. arXiv: 0907.3721. URL: http://dx.doi.org/10.1038/nnano.2009.267.

[62] A Eichler et al. "Ultrasensitive force detection with a nanotube mechanical resonator". In: 8.June (2013), pp. 493–496. DOI: 10.1038/nnano.2013.97.

[63] J Chaste et al. "A nanomechanical mass sensor with yoctogram resolution." In: *Nature nanotechnology* 7.5 (2012), pp. 301–4. ISSN: 1748-3395. DOI: 10.1038/nnano.2012.42. URL: http://www.ncbi.nlm.nih.gov/pubmed/22466856.

[64] Chang-Hua Liu, In Soo Kim, and Lincoln J. Lauhon. "Optical Control of Mechanical Mode-Coupling within a MoS ₂ Resonator in the Strong-Coupling Regime". In: *Nano Letters* 15.10 (2015), pp. 6727–6731. ISSN: 1530-6984. DOI: 10.1021/acs.nanolett.5b02586. URL: http://pubs.acs.org/doi/10.1021/acs.nanolett.5b02586.

[65] C. Samanta, P. R. Yasasvi Gangavarapu, and A. K. Naik. "Nonlinear mode coupling and internal resonances in MoS2nanoelectromechanical system". In: *Applied Physics Letters* 107.17 (2015). ISSN: 00036951. DOI: 10.1063/1.4934708.

[66] R. Van Leeuwen et al. "Time-domain response of atomically thin MoS2 nanomechanical resonators". In: *Applied Physics Letters* 105.4 (2014). ISSN: 00036951. DOI: 10.1063/1.4892072. arXiv: arXiv:1405.5666v1.

[67] Jaesung Lee et al. "Air damping of atomically thin MoS2 nanomechanical resonators". In: *Applied Physics Letters* 105.2 (2014). ISSN: 00036951. DOI: 10.1063/1.4890387.

[68] AC Gomez et al. "Single-layer MoS2 mechanical resonator". In: *Adv. Mater* 25 (2013), pp. 6719–23.

[69] Shamashis Sengupta et al. "Electromechanical resonators as probes of the charge density wave transition at the nanoscale in NbSe2". In: *Physical Review B - Condensed Matter and Materials Physics* 82.15 (2010), pp. 1–5. ISSN: 10980121. DOI: 10.1103/PhysRevB.82.155432. arXiv: 1004.3453.

[70] Gary A Steele et al. "Strong coupling between single-electron tunneling and nanomechanical motion". In: *Science* 325.5944 (2009), pp. 1103–1107.

[71] Adrien Allain and Andras Kis. "Electron and hole mobilities in single-layer WSe2". In: *ACS Nano* 8.7 (2014), pp. 7180–7185. ISSN: 1936086X. DOI: 10.1021/nn5021538.

[72] Xu Cui et al. "Multi-terminal transport measurements of MoS2 using a van der Waals heterostructure device platform". In: *Nature Nanotechnology* 10.6 (2015), pp. 534–540. ISSN: 1748-3387. DOI: 10.1038/nnano.2015.70. arXiv: 1412.5977. URL: http://www.nature.com/doifinder/10.1038/nnano.2015.70.

[73] Wenzhong Bao et al. “Controlled ripple texturing of suspended graphene and ultrathin graphite membranes”. In: *Nature Nanotechnology* 4.9 (2009), pp. 562–566. ISSN: 17483395. DOI: 10.1038/nnano.2009.191. arXiv: 0903.0414. URL: http://dx.doi.org/10.1038/nnano.2009.191.

[74] Laura G. Remus, Miles P. Blencowe, and Yukihiro Tanaka. “Damping and decoherence of a nanomechanical resonator due to a few two-level systems”. In: *Physical Review B - Condensed Matter and Materials Physics* 80.17 (2009), pp. 28–31. ISSN: 10980121. DOI: 10.1103/PhysRevB.80.174103. arXiv: 0907.0431.

[75] Matthias Imboden and Pritiraj Mohanty. “Dissipation in nanoelectromechanical systems”. In: *Physics Reports* 534.3 (2014), pp. 89–146. ISSN: 03701573. DOI: 10.1016/j.physrep.2013.09.003. URL: http://dx.doi.org/10.1016/j.physrep.2013.09.003.

[76] Christin Edblom and Andreas Isacsson. “Diffusion-induced dissipation and mode coupling in nanomechanical resonators”. In: *Physical Review B - Condensed Matter and Materials Physics* 90.15 (2014), pp. 1–8. ISSN: 1550235X. DOI: 10.1103/PhysRevB.90.155425. arXiv: 1406.1365.

[77] Jin Wu Jiang, Harold S. Park, and Timon Rabczuk. “MoS2 nanoresonators: Intrinsically better than graphene?” In: *Nanoscale* 6.7 (2014), pp. 3618–3625. ISSN: 20403372. DOI: 10.1039/c3nr05991j. arXiv: 1401.0576.

[78] E. Kramer et al. “Strain-dependent damping in nanomechanical resonators from thin MoS ₂ crystals”. In: *Applied Physics Letters* 107.9 (2015), p. 091903. ISSN: 0003-6951. DOI: 10.1063/1.4929507. arXiv: arXiv:1509.03080v1. URL: http://aip.scitation.org/doi/10.1063/1.4929507.

[79] Quirin P. Unterreithmeier, Thomas Faust, and Jörg P. Kotthaus. “Damping of nanomechanical resonators”. In: *Physical Review Letters* 105.2 (2010), pp. 1–4. ISSN: 00319007. DOI: 10.1103/PhysRevLett.105.027205. arXiv: 1003.1868.

[80] Scott S. Verbridge et al. “High quality factor resonance at room temperature with nanostrings under high tensile stress”. In: *Journal of Applied Physics* 99.12 (2006). ISSN: 00218979. DOI: 10.1063/1.2204829.

[81] MI Dykman and MA Krivoglaz. “Classical theory of nonlinear oscillators interacting with a medium”. In: *physica status solidi (b)* 48.2 (1971), pp. 497–512.

[82] A. Eichler et al. “Symmetry breaking in a mechanical resonator made from a carbon nanotube”. In: *Nature Communications* 4 (2013), pp. 1–7. ISSN: 20411723. DOI: 10.1038/ncomms3843. arXiv: 1311.6589.

[83] Arthur W. Barnard et al. "Entropic Spectral Broadening in Carbon Nanotube Resonators". In: 18 (2011), pp. 18–21. DOI: 10.1073/pnas.1216407109. arXiv: 1110.1517. URL: http://arxiv.org/abs/1110.1517{\%}0Ahttp://dx.doi.org/10.1073/pnas.1216407109.

[84] B. P. Abbott et al. "Observation of gravitational waves from a binary black hole merger". In: *Physical Review Letters* 116.6 (2016), pp. 1–16. ISSN: 10797114. DOI: 10.1103/PhysRevLett.116.061102. arXiv: 1602.03837.

[85] JE Losby et al. "Torque-mixing magnetic resonance spectroscopy". In: *Science* 350.6262 (2015), pp. 798–801.

[86] A. Mehlin et al. "Stabilized Skyrmion Phase Detected in MnSi Nanowires by Dynamic Cantilever Magnetometry". In: *Nano Letters* 15.7 (2015), pp. 4839–4844. ISSN: 15306992. DOI: 10.1021/acs.nanolett.5b02232.

[87] AC Bleszynski-Jayich. "AC Bleszynski-Jayich, WE Shanks, B. Peaudecerf, E. Ginossar, F. von Oppen, L. Glazman, and JGE Harris, Science 326, 272 (2009)." In: *Science* 326 (2009), p. 272.

[88] Avishai Benyamini et al. "Real-space tailoring of the electron–phonon coupling in ultraclean nanotube mechanical resonators". In: *Nature Physics* 10.2 (2014), p. 151.

[89] Nianbei Li et al. "Colloquium: Phononics: Manipulating heat flow with electronic analogs and beyond". In: *Reviews of Modern Physics* 84.3 (2012), pp. 1045–1066. ISSN: 00346861. DOI: 10.1103/RevModPhys.84.1045. arXiv: 1108.6120.

[90] Gerrit EW Bauer, Eiji Saitoh, and Bart J Van Wees. "Spin caloritronics". In: *Nature materials* 11.5 (2012), p. 391.

[91] Jukka P. Pekola. "Towards quantum thermodynamics in electronic circuits". In: *Nature Physics* 11.2 (2015), pp. 118–123. ISSN: 17452481. DOI: 10.1038/nphys3169.

[92] Myung Ho Bae et al. "Ballistic to diffusive crossover of heat flow in graphene ribbons". In: *Nature Communications* 4 (2013). ISSN: 20411723. DOI: 10.1038/ncomms2755. arXiv: arXiv:1507.02142v2.

[93] N. Morell et al. "High Quality Factor Mechanical Resonators Based on WSe_2 Monolayers". In: *Nano Letters* 8 (). ISSN: 15306992. DOI: 10.1021/acs.nanolett.6b02038.

[94] J Hone et al. "Quantized phonon spectrum of single-wall carbon nanotubes". In: *Science* 289.5485 (2000), pp. 1730–1733.

[95] Harmas L Kiwia and Edgar F Westrum Jr. "Low-temperature heat capacities of molybdenum diselenide and ditelluride". In: (1975).

[96] Giorgia Fugallo et al. “Ab initio variational approach for evaluating lattice thermal conductivity”. In: 045430 (2012), pp. 1–9. ISSN: 1098-0121. DOI: 10.1103/PhysRevB.88.045430. arXiv: 1212.0470. URL: http://arxiv.org/abs/1212.0470{\%}0Ahttp://dx.doi.org/10.1103/PhysRevB.88.045430.

[97] Sangyeop Lee et al. “Hydrodynamic phonon transport in suspended graphene”. In: *Nature communications* 6 (2015), p. 6290.

[98] Stefano Lepri, Roberto Livi, and Antonio Politi. “Thermal conduction in classical low-dimensional lattices”. In: *Physics Reports* 377.1 (2003), pp. 1–80. ISSN: 03701573. DOI: 10.1016/S0370-1573(02)00558-6. arXiv: 0112193 [cond-mat].

[99] L. Lindsay et al. “Phonon thermal transport in strained and unstrained graphene from first principles”. In: *Physical Review B - Condensed Matter and Materials Physics* 89.15 (2014), pp. 1–8. ISSN: 1550235X. DOI: 10.1103/PhysRevB.89.155426.

[100] Xiaoxiang Xi et al. “Strongly enhanced charge-density-wave order in monolayer NbSe 2”. In: *Nature Nanotechnology* 10.9 (2015), pp. 765–769. ISSN: 17483395. DOI: 10.1038/nnano.2015.143. arXiv: 1507.05595. URL: http://dx.doi.org/10.1038/nnano.2015.143.

[101] VK Thorsmølle et al. “C-axis Josephson plasma resonance observed in Tl 2 Ba 2 CaCu 2 O 8 superconducting thin films by use of terahertz time-domain spectroscopy”. In: *Optics letters* 26.16 (2001), pp. 1292–1294.